NASA TM X-453

TECHNICAL MEMORANDUM

X-453

EXPERIMENTAL INVESTIGATION OF PRESSURE DISTRIBUTION AND STATIC AERODYNAMIC CHARACTERISTICS FOR THREE SUPERSONIC-IMPACT BALLISTIC REENTRY SHAPES AT MACH NUMBERS OF 1.93, 2.55, AND 3.05

By Odell A. Morris and Arvid L. Keith, Jr.

Langley Research Center
Langley Field, Va.

NATIONAL AERONAUTICS AND SPACE ADMINISTRATION
WASHINGTON
March 1961

NATIONAL AERONAUTICS AND SPACE ADMINISTRATION

TECHNICAL MEMORANDUM X-453

EXPERIMENTAL INVESTIGATION OF PRESSURE DISTRIBUTION AND STATIC AERODYNAMIC CHARACTERISTICS FOR THREE SUPERSONIC-IMPACT BALLISTIC REENTRY SHAPES AT MACH NUMBERS OF 1.93, 2.55, AND 3.05*

By Odell A. Morris and Arvid L. Keith, Jr.

SUMMARY

An investigation of the pressure distribution and the static aerodynamic characteristics of three ballistic reentry shapes designed to impact at supersonic speeds has been conducted in the Langley 9- by 12-inch blowdown tunnel. The tests were conducted for angles of attack from -4° to 12° for Mach numbers of 1.93, 2.55, and 3.05 and Reynolds numbers of approximately 7.9×10^6, 6.8×10^6, and 5.2×10^6 based on body length. The models varied in nose bluntness and afterbody flare angle and length.

In general, the experimental pressure distributions at zero angle of attack showed good agreement with those predicted by the modified Newtonian theory for all models, the exception being caused by local overexpansion around the corners of the models and effects of shock boundary-layer interaction in the flared region of the afterbody.

Results of the force measurements indicated that all of the models were statically stable and that the model with the 20° truncated-cone forebody and an afterbody flare angle of 3.87° had the lowest minimum drag coefficient at a Mach number of 2.55.

INTRODUCTION

The National Aeronautics and Space Administration and other agencies have been conducting research on the aerodynamic characteristics and heat-transfer ratios of various bodies of revolution with an aim to

develop nose and body shapes which will be suitable for stable atmospheric reentry from ballistic type flight paths. (For example, see refs. 1 to 5.) References 6 to 9 contribute information from subsonic to supersonic speeds for several reentry configurations designed to have drag coefficients low enough to impact at supersonic speeds. As a part of this same program, the present paper presents the pressure distribution on three of the nose-cone configurations of reference 9, and extends the static aerodynamic data of reference 9 to include drag. The investigation was conducted in the 9- by 12-inch blowdown tunnel at Mach numbers of 1.93, 2.55, and 3.05 for an angle-of-attack range of -4° to 12°.

SYMBOLS

The coefficients presented in this paper are based on the wind axis system as indicated in the following sketch:

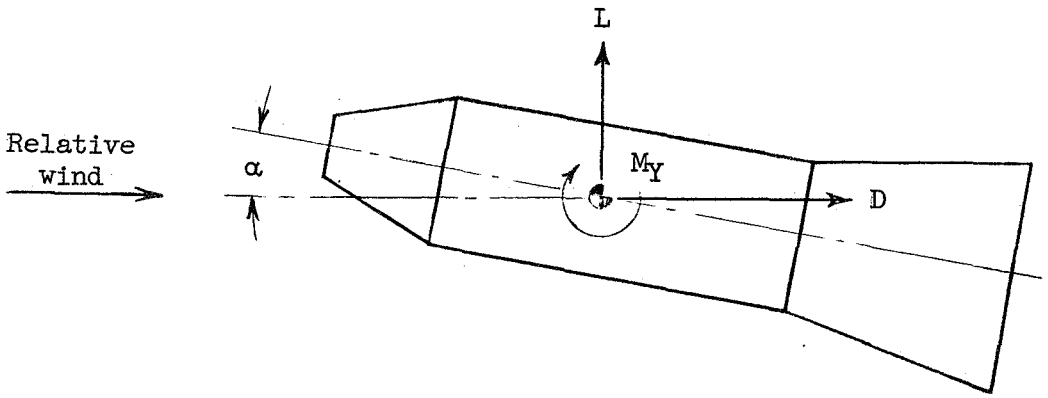

A reference body cross-sectional area, $\frac{\pi d^2}{4}$, sq ft

C_D drag coefficient, $\frac{D}{q_\infty A}$

C_L lift coefficient, $\frac{L}{q_\infty A}$

C_m pitching-moment coefficient (measured at $x/l = 0.398$ for models 1 and 3 and at $x/l = 0.422$ for model 4), $\frac{M_Y}{q_\infty Ad}$

C_p	pressure coefficient, $\frac{p_l - p_\infty}{q_\infty}$
D	drag, lb
d	reference diameter, 1.741 in.
L	lift, lb
l	length of model, in.
M	free-stream Mach number
M_Y	pitching moment, ft-lb
p_l	local static pressure, lb/sq ft
$p_{t,2}$	total pressure behind normal shock, lb/sq ft
p_∞	free-stream static pressure, lb/sq ft
q_∞	free-stream dynamic pressure, lb/sq ft
r	radius of model front face, in.
x	distance measured along horizontal axis from model nose, in.
y	distance measured along vertical axis from model center line, in.
α	angle of attack, deg

APPARATUS AND METHODS

Models

The principal dimensions of the models and the location of the pressure orifices are shown in figure 1. A photograph of model 1 mounted on the tunnel sting-support system is shown in figure 2. The blunt-nose-cone cylindrical-flared bodies, which were designed for supersonic impact, are referred to as models 1, 3, and 4, which are the same designations as in references 7 and 9. Tests on model 2 were omitted from the present investigation. Models 1 and 3 have the same truncated-cone nose shape but differ in the cylindrical-center-body

length and afterbody flare angle. Model 4 differs from model 3 only in that it has a longer nose; consequently, model 4 has a reduced nose diameter. All three models were constructed of aluminum and were sting mounted from a movable strut within the tunnel.

Tests and Measurements

The investigation was conducted in the Langley 9- by 12-inch blow-down tunnel at Mach numbers of 1.93, 2.55, and 3.05. The stagnation pressure at $M = 1.93$ was 40 lb/sq in. abs, and at Mach numbers of 2.55 and 3.05 the stagnation pressure was 50 lb/sq in. abs. The three Mach numbers were obtained by using interchangeable nozzle blocks for fixed Mach numbers. The Reynolds number based on body length was approximately 7.9×10^6 at $M = 1.93$, 6.8×10^6 at $M = 2.55$, and 5.2×10^6 at $M = 3.05$. The sting-support system was attached to a plate in the tunnel floor which rotated to permit angle-of-attack variation. For the pressure measurements, the pressure tubes were brought out through the inside of the sting and strut through the tunnel floor. For the force measurements, which were conducted at Mach numbers 2.55 and 3.05, the models were sting mounted on a six-component strain-gage balance. Tests at a Mach number of 1.93 with the use of this sting support were omitted due to interference effects caused by shock reflections from the model nose off the tunnel wall as can be seen in figure 3.

The angle of attack was corrected for sting and balance deflection under load and for a tunnel downflow angle of 0.05 at a Mach number of 3.05. Drag of the models includes the base pressure drag as measured by the balance. The sting interference effects for the ratio of the sting diameter to base diameter for the present configuration have been shown to have insignificant effect on base pressure drag (ref. 10). Transition was fixed on all of the models at the 0.75 radius of the front face with the use of No. 180 carborundum grains as determined in reference 9.

The estimated maximum errors of the data presented in this paper are as follows:

C_p	±0.01
C_D	±0.01
C_L	±0.02
C_m	±0.01
M	±0.02
α, deg	±0.10

PRESENTATION OF DATA

The pressure distributions are plotted in terms of the ratio of the local pressure on the surface of the model to the normal shock total pressure $p_l/p_{t,2}$ as a function of the nondimensional contour lengths (y/r for the blunt-nose section and x/l for the body length) in figures 4 to 6. A comparison of the pressures for the three models plotted in the form of pressure coefficients at zero angle of attack are presented in figure 7. Figure 8 shows a comparison of the experimental pressure coefficients and the theoretical pressure coefficients for the models at zero angle of attack. The force measurements, which include the lift, drag, and pitching-moment coefficients for the models, are presented in figure 9 plotted against angle of attack. The base pressure coefficients of the models plotted against angle of attack are presented in figure 10.

DISCUSSION OF RESULTS

Pressure Measurements

In general, for all of the models tested, a decrease in pressure occurred over the blunt-nose surface when moving toward the outer edge of the nose from the stagnation point at zero angle of attack (fig. 7). Around the sharp corner connecting the blunt nose and the conical section, a rapid acceleration of the flow appears to produce a localized overexpansion at the start of the conical section. (See the schlieren photographs of fig. 3.) The strongest overexpansion occurs at the lower Mach numbers. Toward the end of the conical section, compression of the flow occurs, and the pressure increases rapidly and approaches that pressure which would exist on a sharp nose cone of the same apex angle. Again, at the corner connecting the conical section and the cylindrical section, a sharp drop in pressure occurs and tends to approach zero toward the end of the cylindrical section. About the only sizable difference in pressures between the models occurred at the juncture of the cylindrical section and the flared section. That is, the pressures on model 1 decreased to zero just ahead of the base; whereas models 3 and 4 produced a pressure rise at the start of the 10° conical flared section.

Increasing angle of attack generally produced an increase in pressures along the bottom surface of the models and a decrease in pressure along the top surface as would be expected. (See figs. 4 to 6.) Effects of angle of attack on the pressures along the sides of the models were small over the conical nose section. However, for models 3 and 4, sizable decreases in pressures occurred toward the rear of the cylindrical center

body and on the afterbody flared section. These decreases in pressure appear to result from vortices rolling up along the sides of the model which originated from the bottom of the model in the region of the conical nose section as the angle of attack was increased.

Theoretical pressures at zero angle of attack obtained by using the modified Newtonian equation as suggested in reference 11 shows good agreement with the experimental values except for the pressures at the corners of the models (fig. 8). In this region the agreement is poor at all Mach numbers which is probably caused by localized overexpansion and compression of the flow around the sharp corners and effects of shock boundary-layer interaction in the flared region of the afterbody.

Force Measurements

The force measurements were made on the models primarily to obtain the drag coefficients which were not measured in the tests of reference 9, and are presented in figure 9, together with the lift and pitching-moment coefficients. Of the three models tested, model 1 with the 3.87° flared sides had the lowest minimum drag coefficient at $M = 2.55$ although the blunt-nose area on model 1 was about 5.3 percent larger than the blunt-nose area on model 4. A comparison of the minimum drag for the three models at $M = 2.55$ indicates that the afterbody skirt flare has a more powerful influence on drag than the blunt-nose size. At $M = 3.05$, it appears that the minimum drag is probably influenced by nose size to a greater extent than afterbody shape as evidenced by the nearly equal minimum drags of models 1 and 4. Thus, at higher Mach numbers, model 4 would be expected to have the lowest minimum drag.

Calculations of the minimum drag coefficient for the three models with the use of the measured pressure coefficients are listed in table I. These values which include the model base pressures and a calculated skin-friction drag coefficient of 0.04 (ref. 12) show good agreement with the experimental values.

The variation of the lift coefficient for the three models with angle of attack was linear up to an angle of attack of about 6° (fig. 9). The pitching-moment curves are more linear at angles of attack near 0° than were shown previously by the data of reference 9. The differences in the pitching-moment curves were probably caused by the different model-mounting test technique used in the tests of reference 9 which may have produced some slight tunnel-interference effects. In any case, as was pointed out in reference 9, the pitching-moment data indicate that all of the models were stable and that model 3 was the most stable of the models investigated.

CONCLUDING REMARKS

An investigation of pressure distribution and the static stability of three ballistic reentry shapes believed to be suitable for supersonic impact has been made at Mach numbers of 1.93, 2.55, and 3.05. In general, the experimental pressure distributions at zero angle of attack showed good agreement with those predicted by the modified Newtonian theory for all models, the exception being caused by local overexpansion around the corners of the models and effects of the shock boundary-layer interaction in the flared region of the afterbody. Results of the force measurements indicated that all of the models were statically stable and that the model with the 20° truncated-cone forebody and an afterbody flare angle of 3.87 had the lowest minimum drag coefficient at a Mach number of 2.55. The measured drag coefficients indicated that at a Mach number of 2.55, the afterbody flare angle had the more powerful influence on minimum drag; however, at a Mach number of 3.05, the area of the blunt nose had a larger effect on drag as predicted by Newtonian theory.

Langley Research Center,
National Aeronautics and Space Administration,
Langley Field, Va., November 14, 1960.

REFERENCES

1. Carter, Howard S., and Bressette, Walter E.: Heat Transfer and Pressure Distribution on Six Blunt Noses at a Mach Number of 2. NACA RM L57C18, 1957.

2. Hasting, S. M., Persh, J., and Redman, E. J.: Experimental Investigation of the Pressure Distribution on Axi-Symmetric Flat-Face Cone-Type Bodies at Supersonic and Hypersonic Speeds. NAVORD Rep. 5659 (Aerodynamic Res. Rep. 3), U.S. Naval Ord. Lab. (White Oaks, Md.), Oct. 1, 1957.

3. Speegle, Katherine C., Chauvin, Leo T., and Heberlig, Jack C.: Heat Transfer for Mach Numbers Up to 2.2 and Pressure Distributions for Mach Numbers up to 4.7 From Flight Investigations of a Flat-Face-Cone and a Hemisphere-Cone. NACA RM L58B18, 1958.

4. Markley, J. Thomas: Heat Transfer and Pressure Measurements on a 5-Inch Hemispherical Concave Nose at a Mach Number of 2.0. NACA RM L58C14a, 1958.

5. Fisher, Lewis R., Keith, Arvid L., Jr., and DiCamillo, Joseph R.: Aerodynamic Characteristics of Some Families of Blunt Bodies at Transonic Speeds. NASA MEMO 10-28-58L, 1958.

6. Gregory, Donald T., and Carraway, Ausley B.: An Investigation at Mach Numbers from 1.47 to 2.87 of Static Stability Characteristics of Nine Nose Cones Designed for Supersonic Impact Velocities. NASA TM X-69, 1959.

7. Mugler, John P., Jr.: Transonic Wind-Tunnel Investigation of the Static Longitudinal Aerodynamic Characteristics of Five Nose Cones Designed for Supersonic Impact. NASA TM X-432, 1961.

8. Fletcher, Herman S., and Wolhart, Walter D.: Damping in Pitch and Static Stability of Supersonic Impact Nose Cones, Short Blunt Subsonic Impact Nose Cones, and Manned Reentry Capsules at Mach Numbers From 1.93 to 3.05. NASA TM X-347, 1960.

9. Swihart, John M.: Static Stability Investigation of Supersonic-Impact Ballistic Reentry Shapes at Mach Numbers of 2.55 and 3.05. NASA MEMO 5-27-59L, 1959.

10. Perkins, Edward W.: Experimental Investigation of the Effects of Support Interference on the Drag of Bodies of Revolution at a Mach Number of 1.5. NACA TN 2292, 1951. (Supersedes NACA RM A8B05.)

11. Oliver, Robert E.: An Experimental Investigation of Flow Over Simple Blunt Bodies at a Nominal Mach Number of 5.8. GALCIT Memo. No. 26 (Contract No. DA-04-495 Ord-19), June 1, 1955.

12. Chapman, Dean R., and Kester, Robert H.: Turbulent Boundary-Layer and Skin-Friction Measurements in Axial Flow Along Cylinders at Mach Numbers Between 0.5 and 3.6. NASA TN 3097, 1954.

TABLE I.- MINIMUM DRAG COEFFICIENTS

Model	Mach number	$(C_D)_{pressure}$	$(C_D)_{base}$	$(C_D)_{friction}$	$(C_D)_{total}$	$(C_D)_{measured}$
1	1.93	0.4552	0.303	0.04	0.7982	-----
	2.55	.4520	.199	.04	.6910	0.685
	3.05	.4392	.191	.04	.6702	.665
3	2.55	0.6016	0.1898	0.04	0.8314	0.820
	3.05	.5336	.1978	.04	.7714	.750
4	2.55	0.4956	0.2170	0.04	0.7526	0.742
	3.05	.4456	.1885	.04	.6741	.666

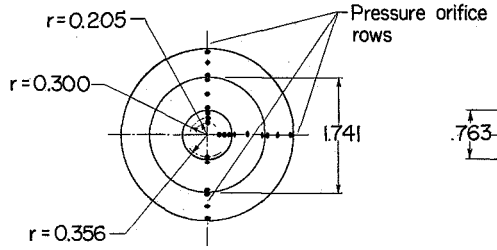

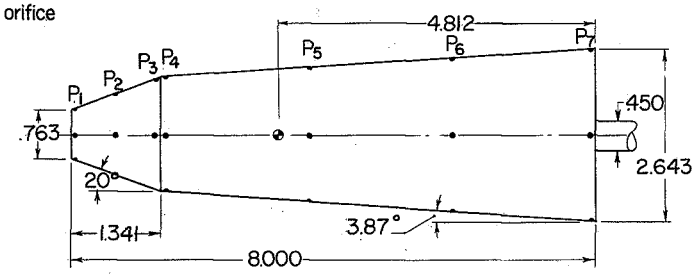

Model 1

Orifice	x, in.	x/l
P_1	.062	.008
* P_2	.670	.084
P_3	1.278	.160
P_4	1.403	.175
P_5	3.581	.448
P_6	5.760	.720
P_7	7.938	.992

Model 1

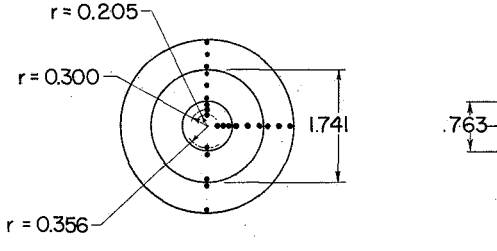

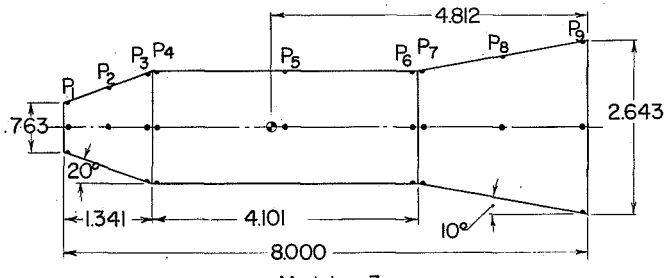

Model 3

Orifice	x, in.	x/l
P_1	.062	.008
* P_2	.670	.084
P_3	1.278	.160
P_4	1.403	.175
* P_5	3.391	.424
P_6	5.379	.672
P_7	5.504	.688
* P_8	6.721	.840
P_9	7.938	.992

Model 3

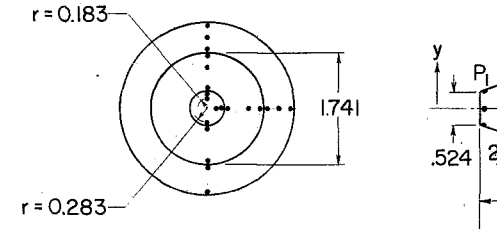

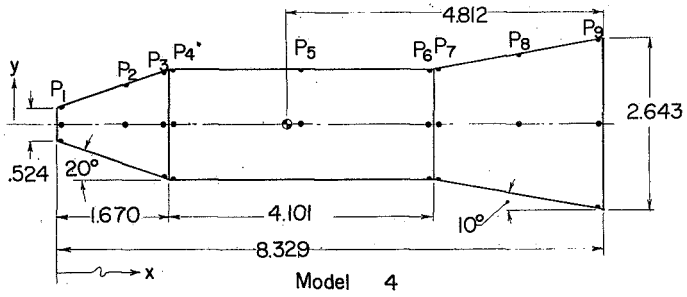

Model 4

Orifice	x, in.	x/l
P_1	.062	.007
* P_2	1.045	.125
P_3	1.607	.193
P_4	1.732	.208
* P_5	3.720	.447
P_6	5.708	.685
P_7	5.833	.700
* P_8	7.050	.846
P_9	8.266	.992

Model 4

* No orifices on bottom row

Figure 1.- Details of models. All dimensions are in inches unless otherwise noted.

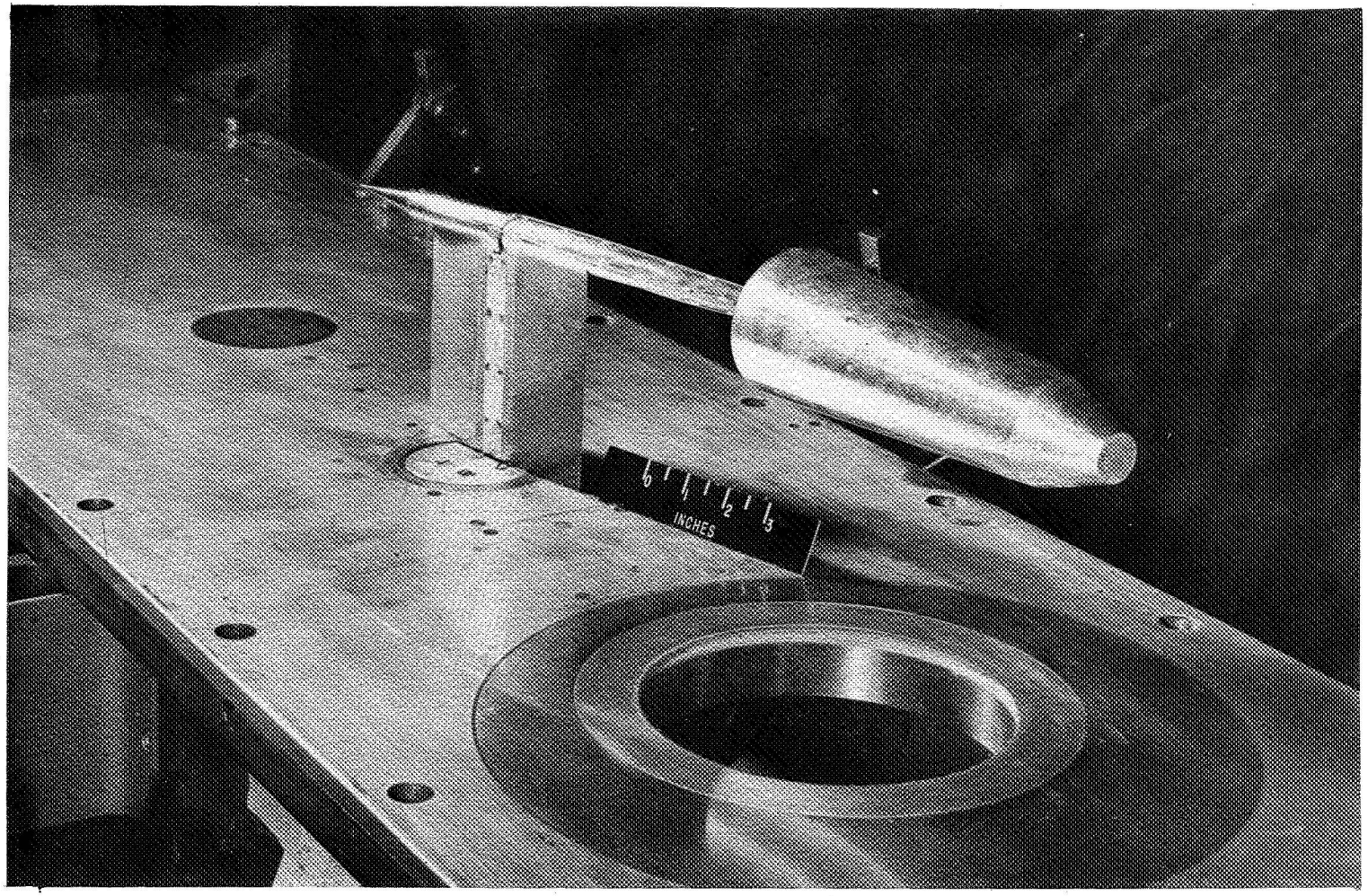

Figure 2.- Photograph of model 1 mounted on sting support. L-58-3305

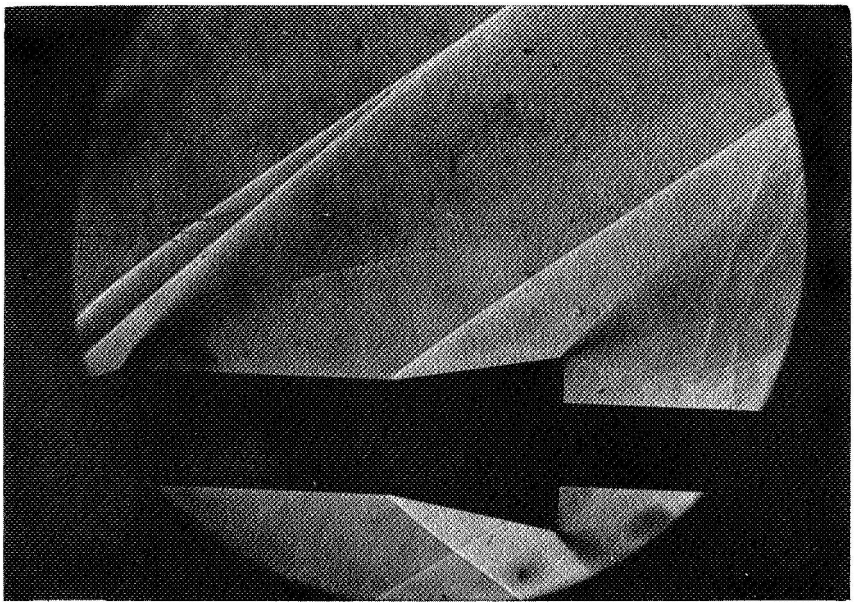

$\alpha = 2°$

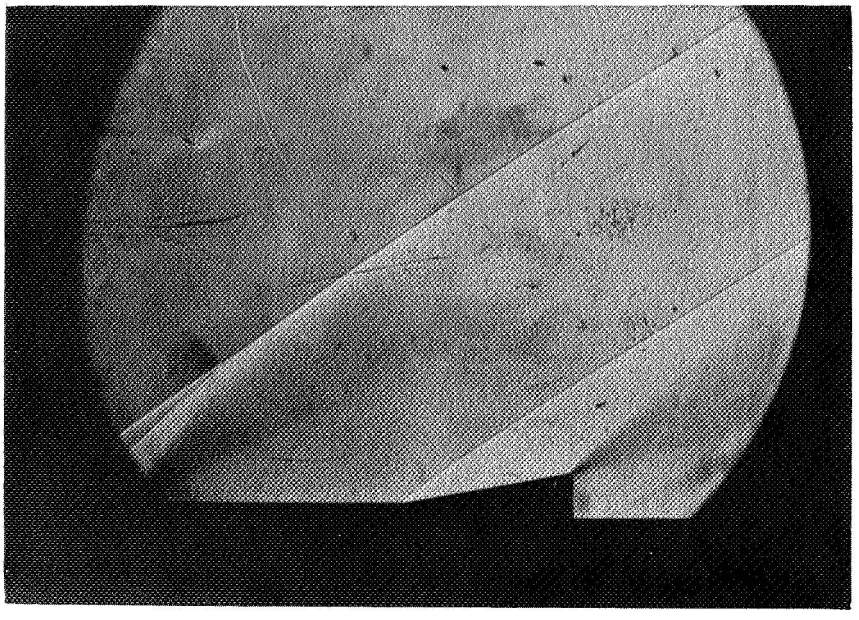

$\alpha = -1°$

L-60-6938

Figure 3.- Schlieren photographs of model 3 at M = 1.93.

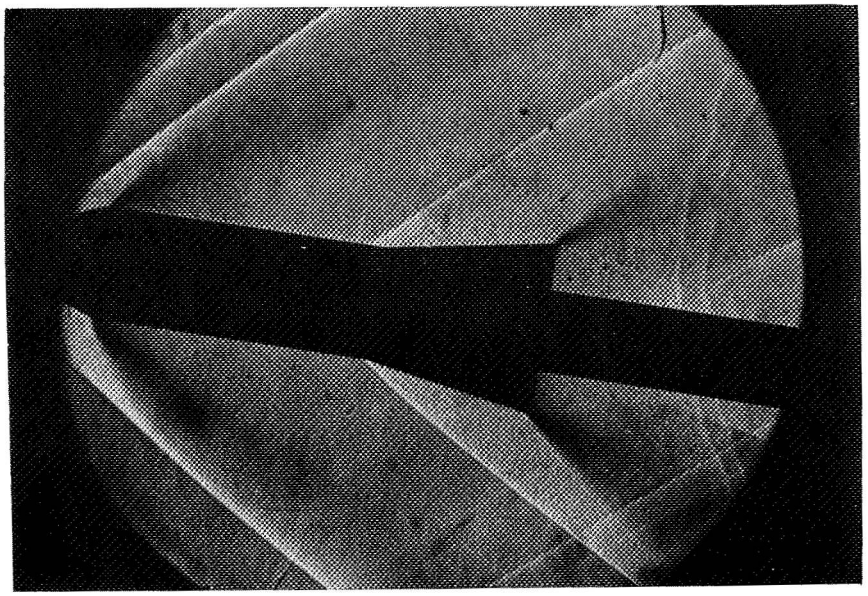

$\alpha = 8°$

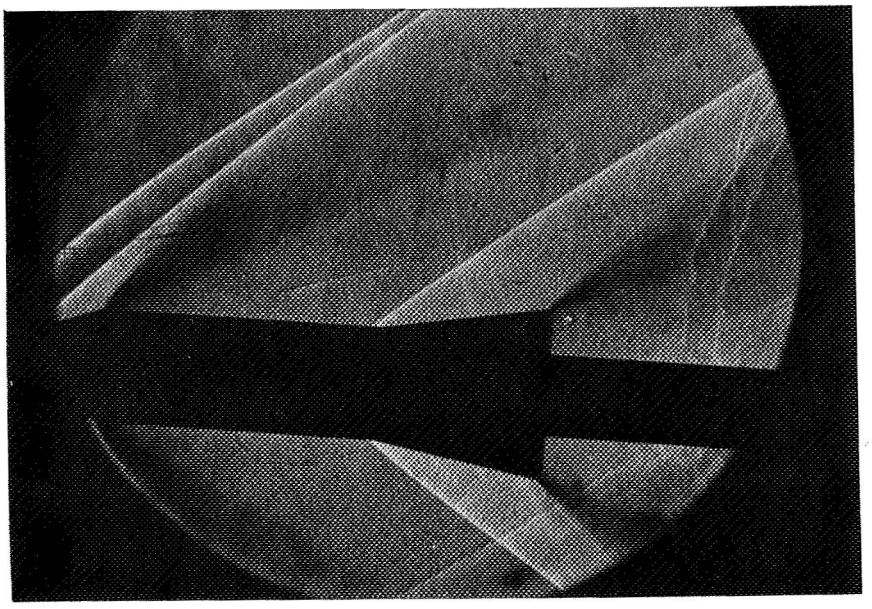

$\alpha = 4.5°$

Figure 3.- Concluded. L-60-6939

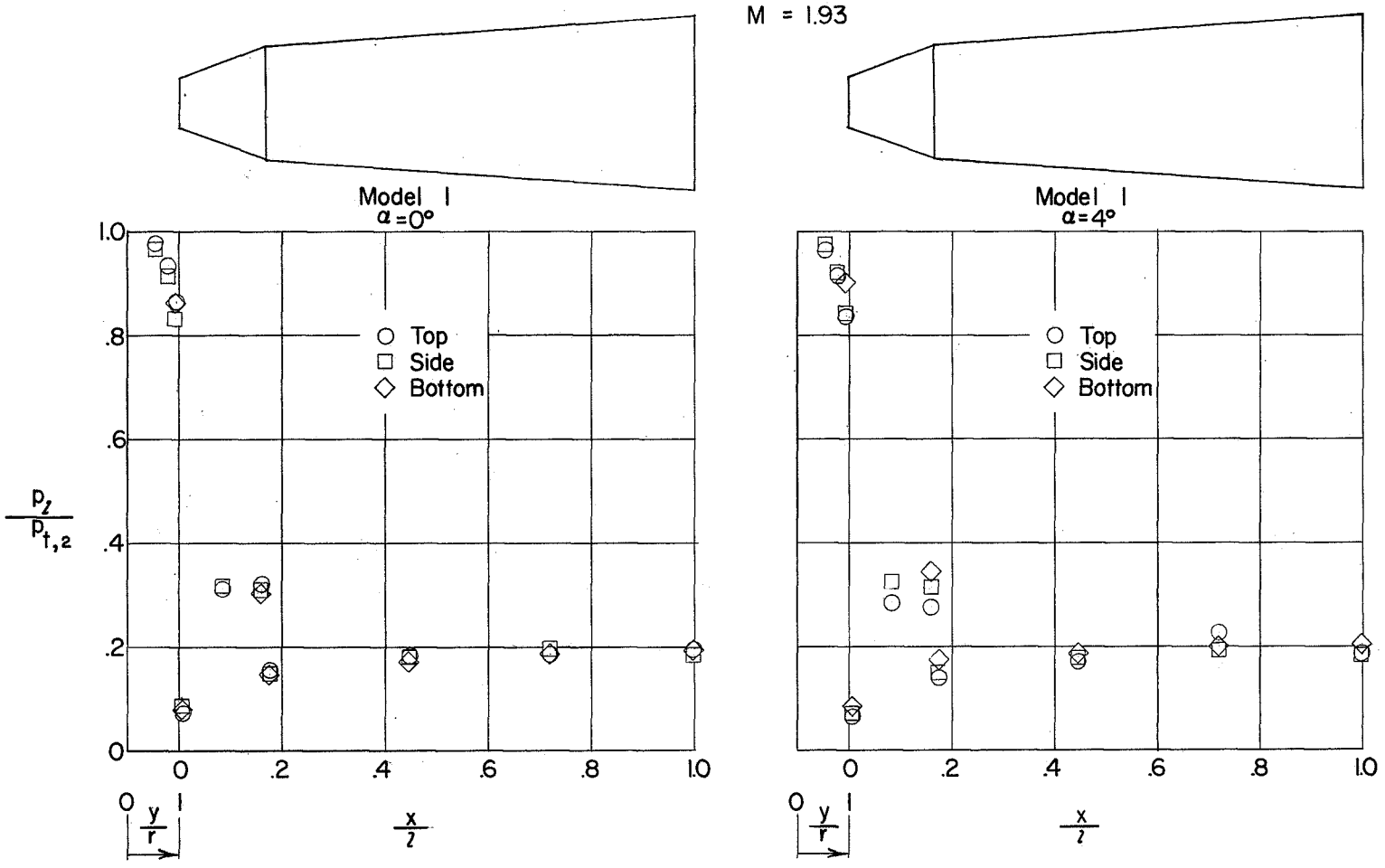

(a) $\alpha = 0^{\circ}$ and 4° at $M = 1.93$.

Figure 4.- Pressure measurements for model 1.

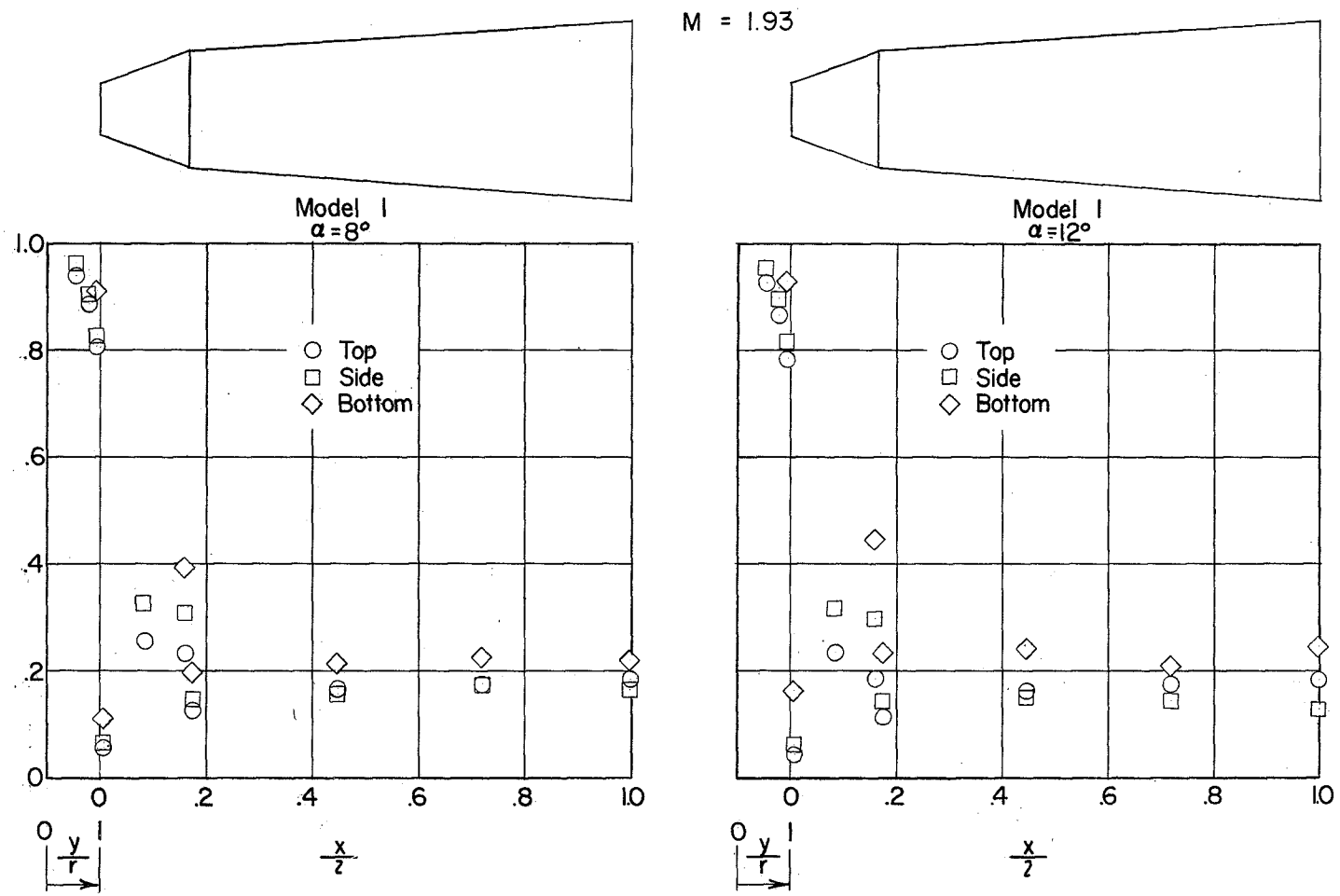

(b) $\alpha = 8^\circ$ and 12° at $M = 1.93$.

Figure 4.- Continued.

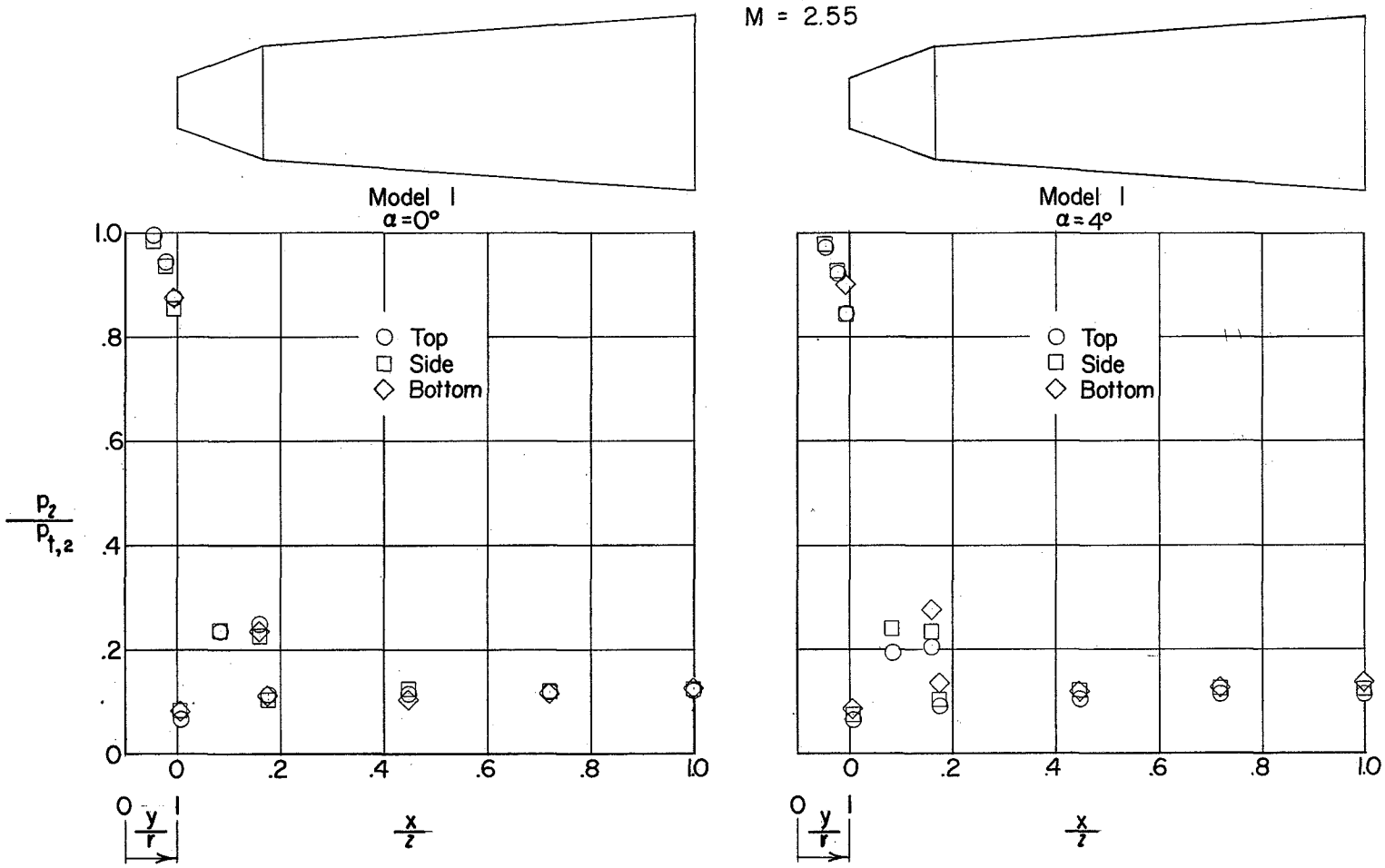

(c) $\alpha = 0^\circ$ and 4° and $M = 2.55$.

Figure 4.- Continued.

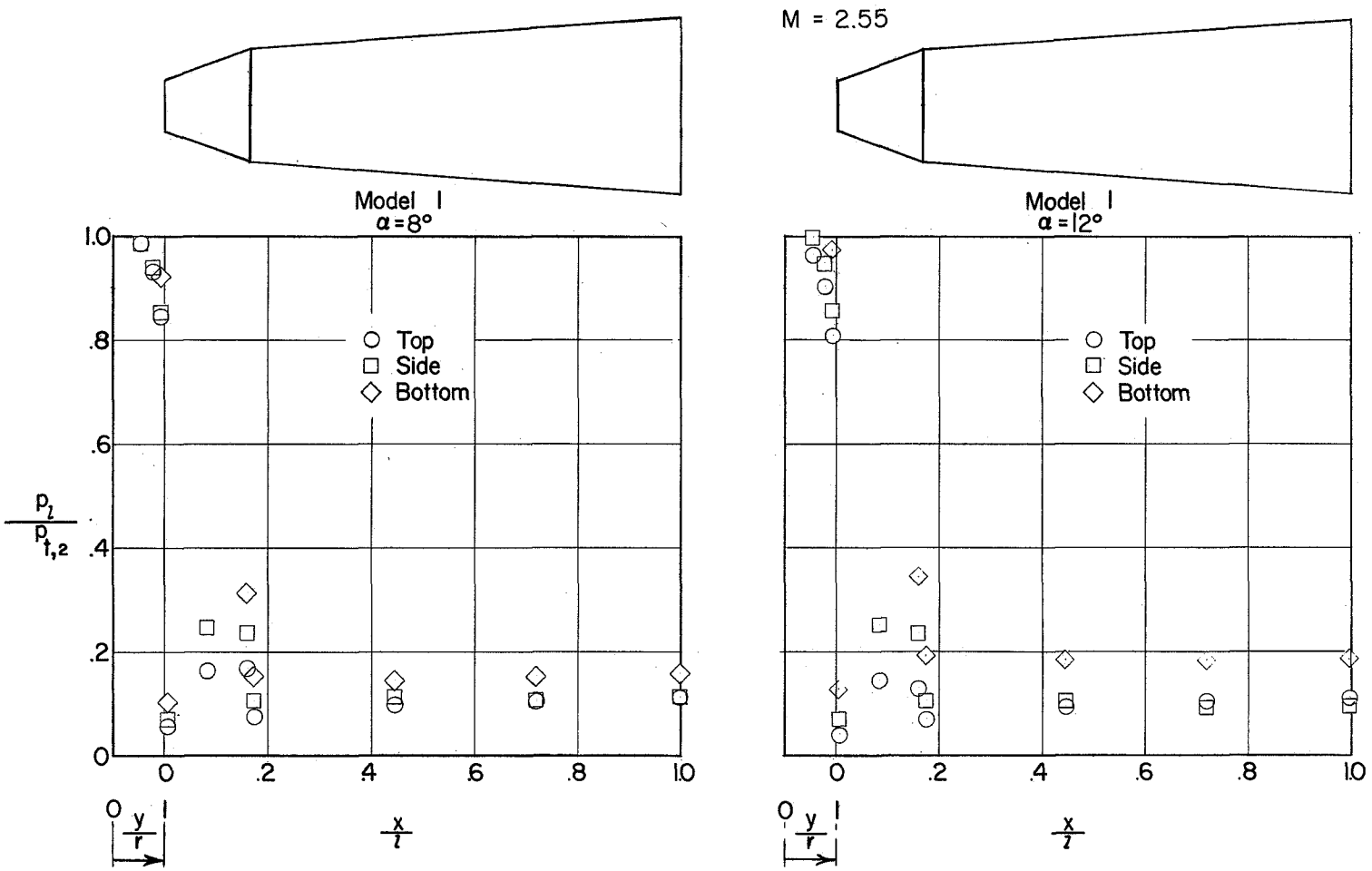

(d) $\alpha = 8^{\circ}$ and 12° at $M = 2.55$.

Figure 4.- Continued.

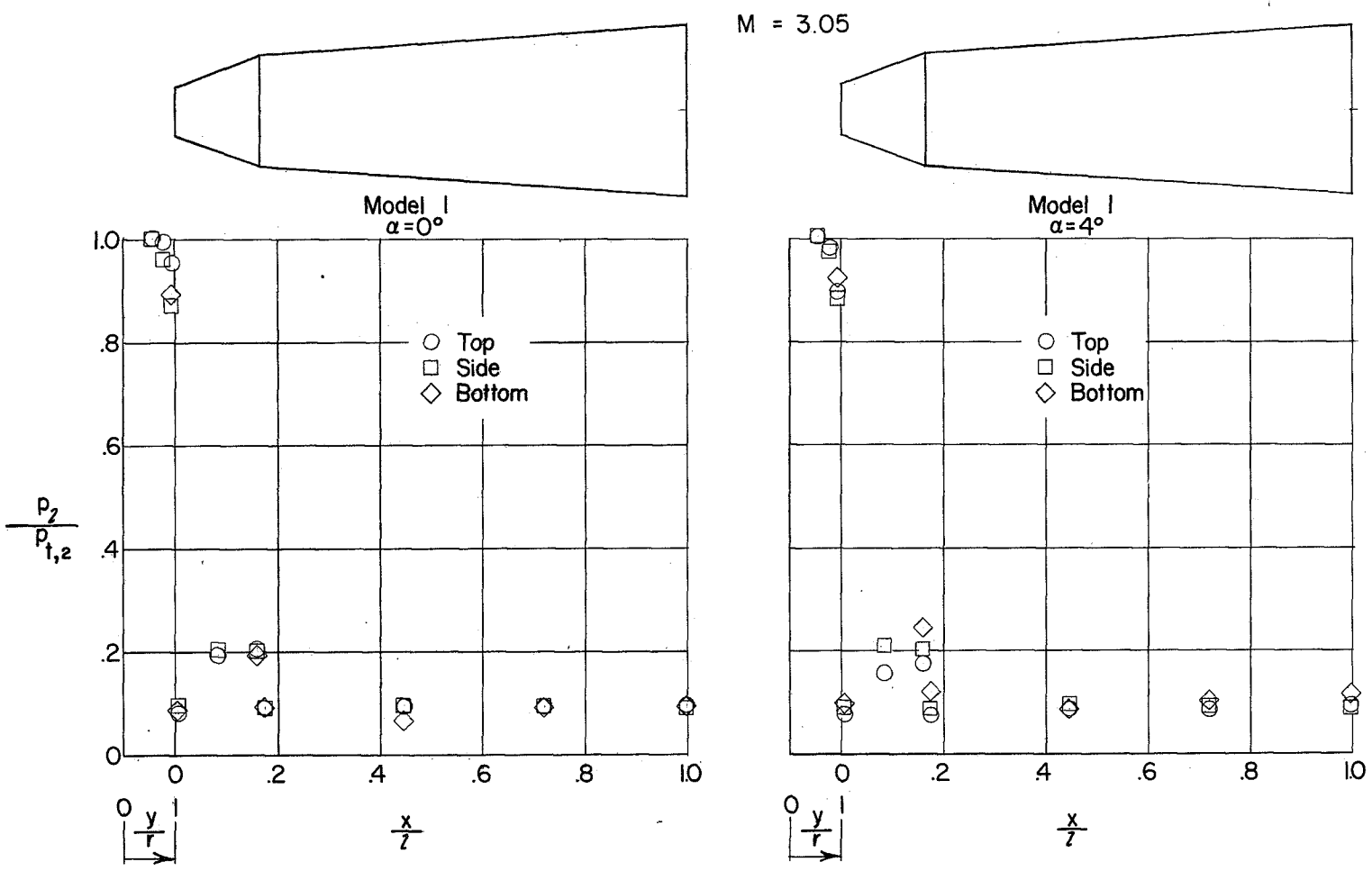

(e) $\alpha = 0^\circ$ and 4° at $M = 3.05$.

Figure 4.- Continued.

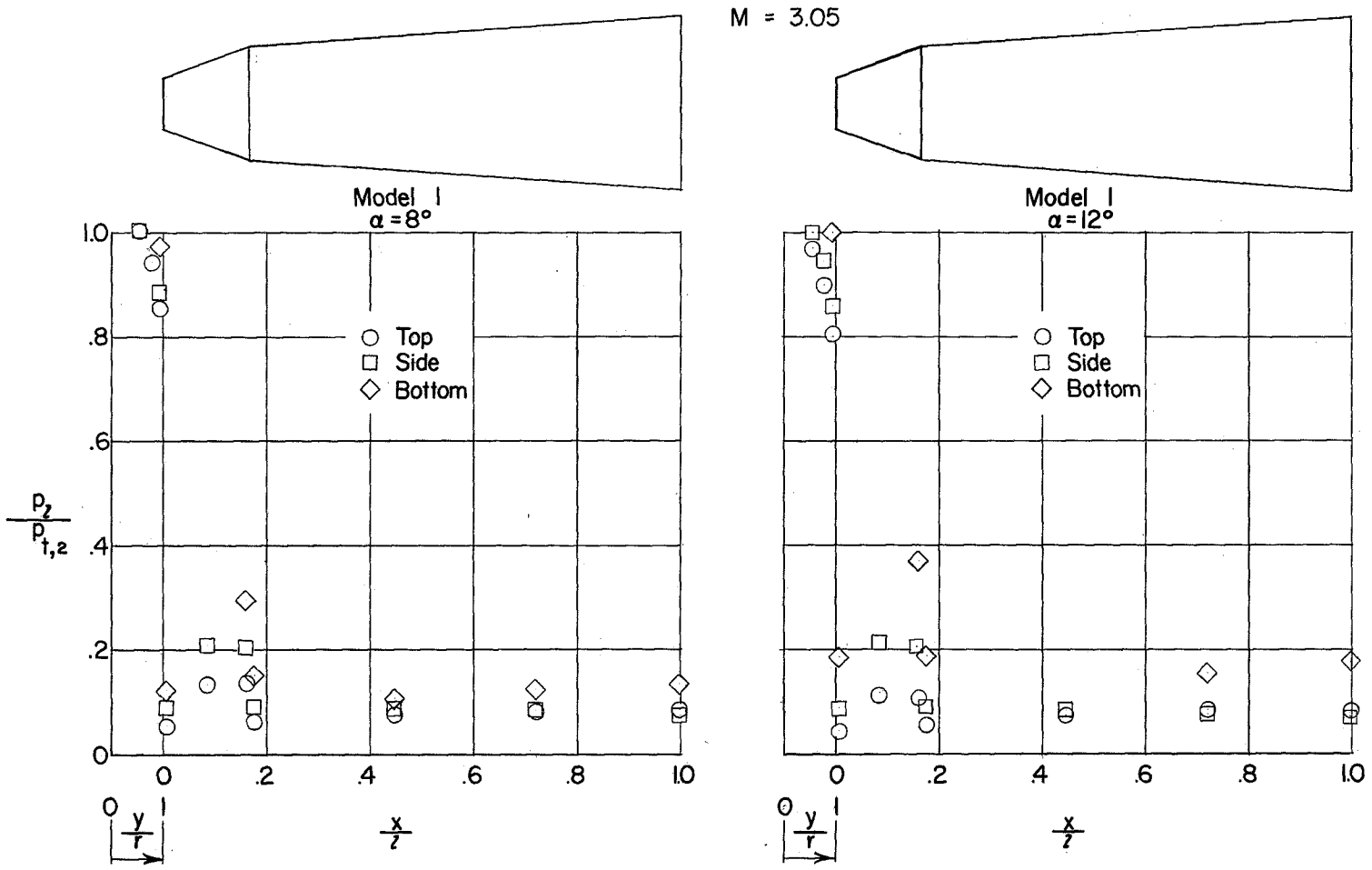

(f) $\alpha = 8^\circ$ and 12° at $M = 3.05$.

Figure 4.- Concluded.

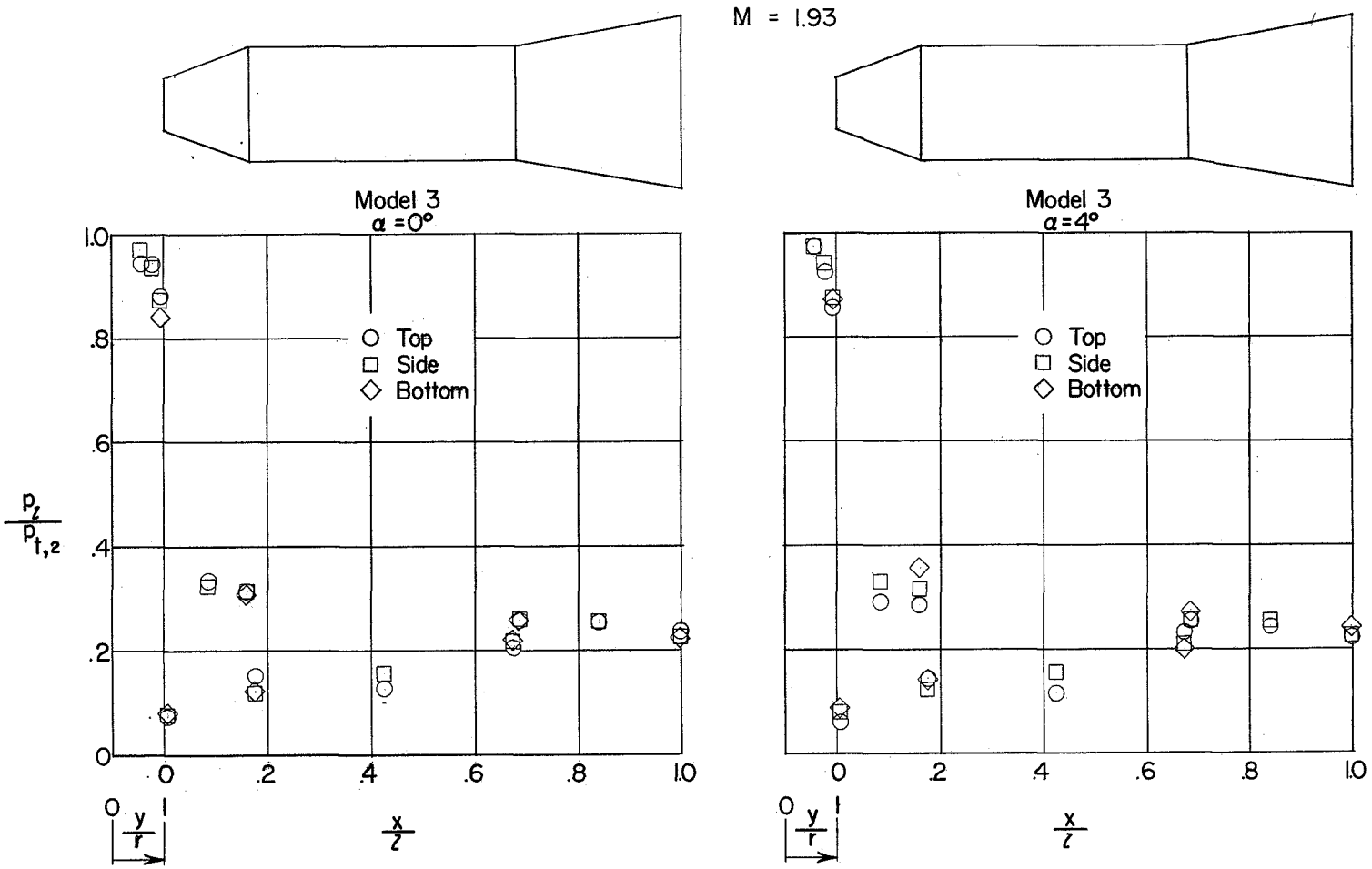

(a) $\alpha = 0^{\circ}$ and 4° at $M = 1.93$.

Figure 5.- Pressure measurements for model 3.

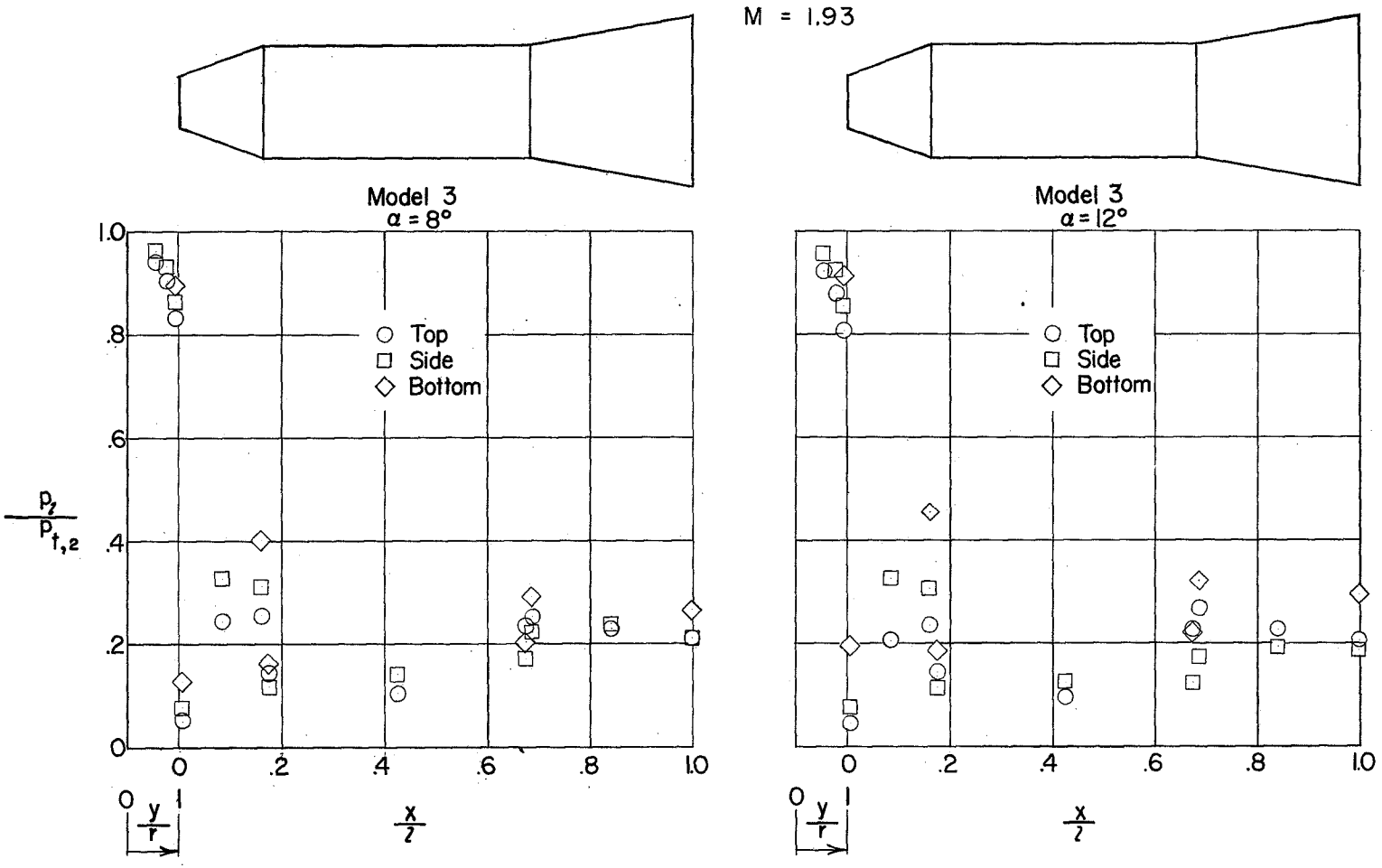

(b) $\alpha = 8^\circ$ and 12° at $M = 1.93$.

Figure 5.- Continued.

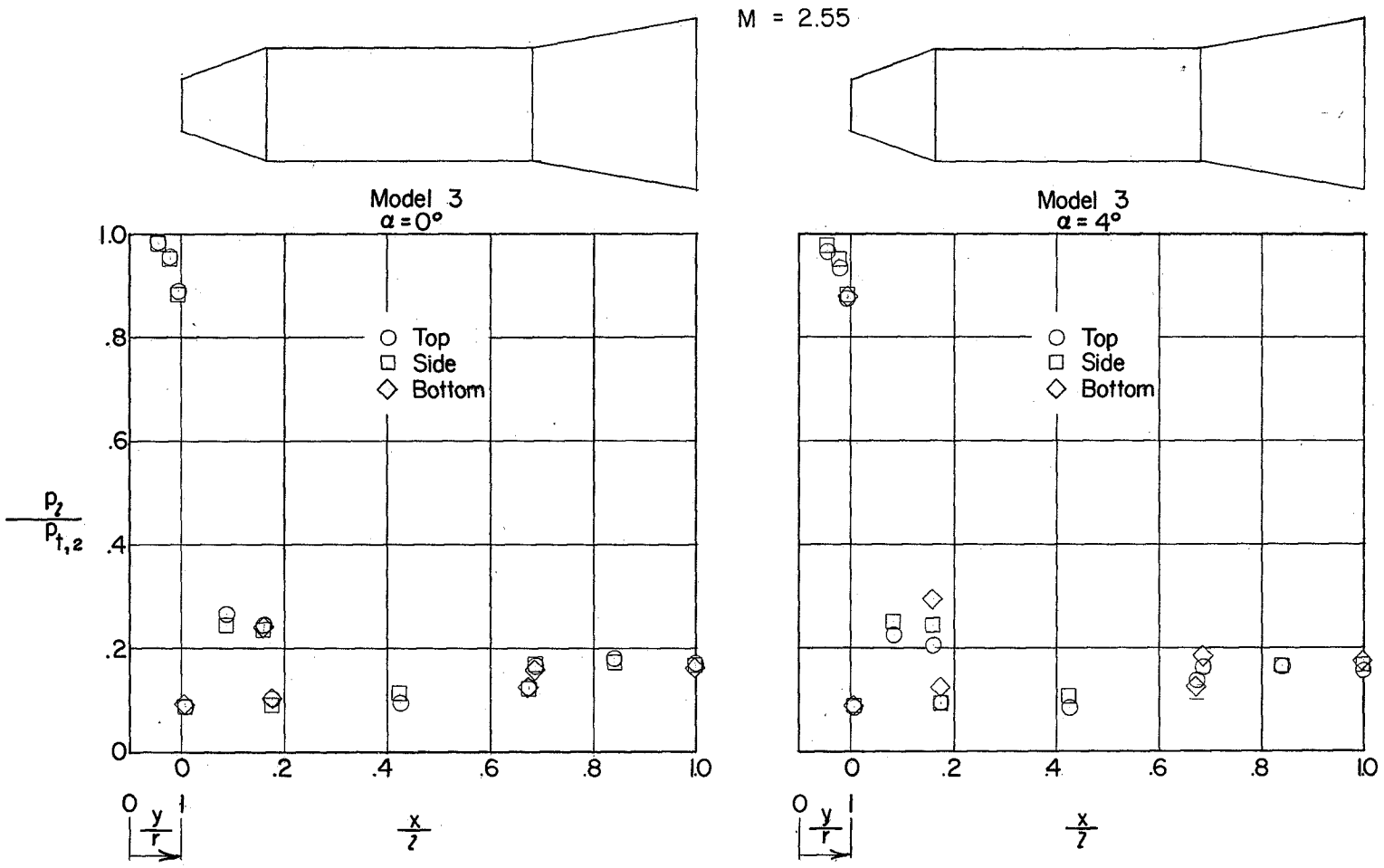

(c) $\alpha = 0^\circ$ and 4° at $M = 2.55$.

Figure 5.- Continued.

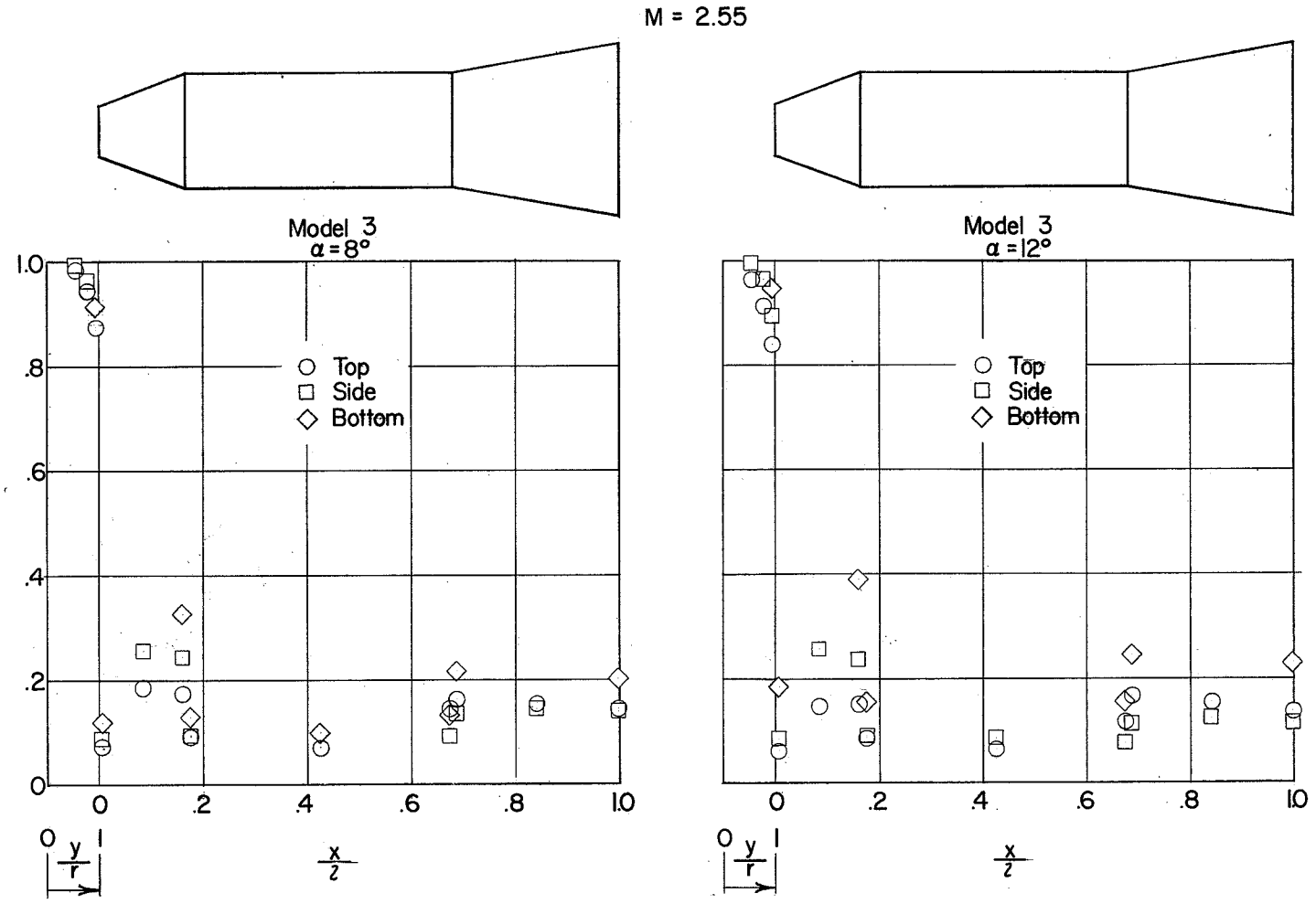

(d) $\alpha = 8^\circ$ and 12° at $M = 2.55$.

Figure 5.- Continued.

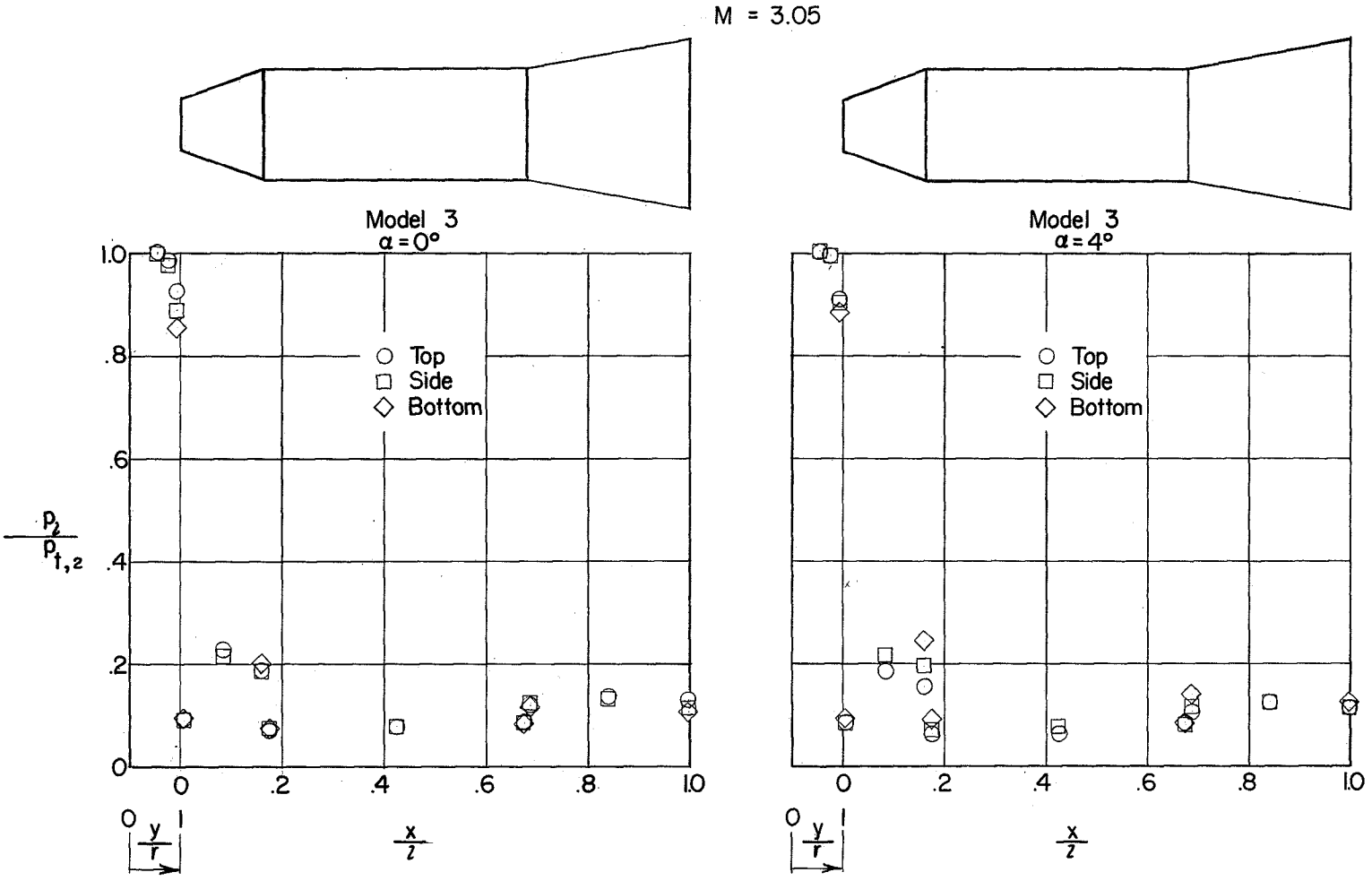

(e) $\alpha = 0^\circ$ and 4° at $M = 3.05$.

Figure 5.- Continued.

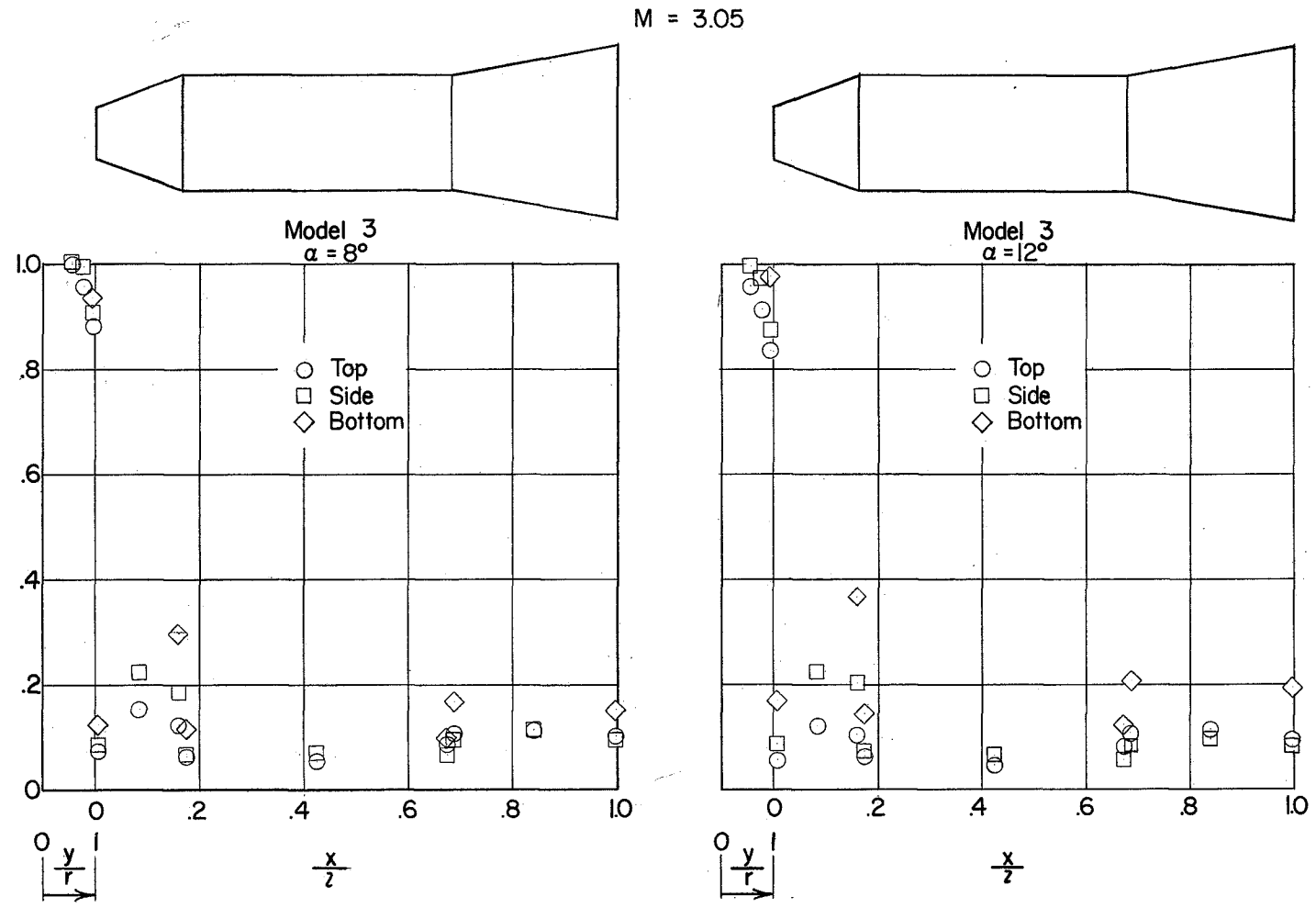

(f) $\alpha = 8^{\circ}$ and 12° at $M = 3.05$.

Figure 5.- Concluded.

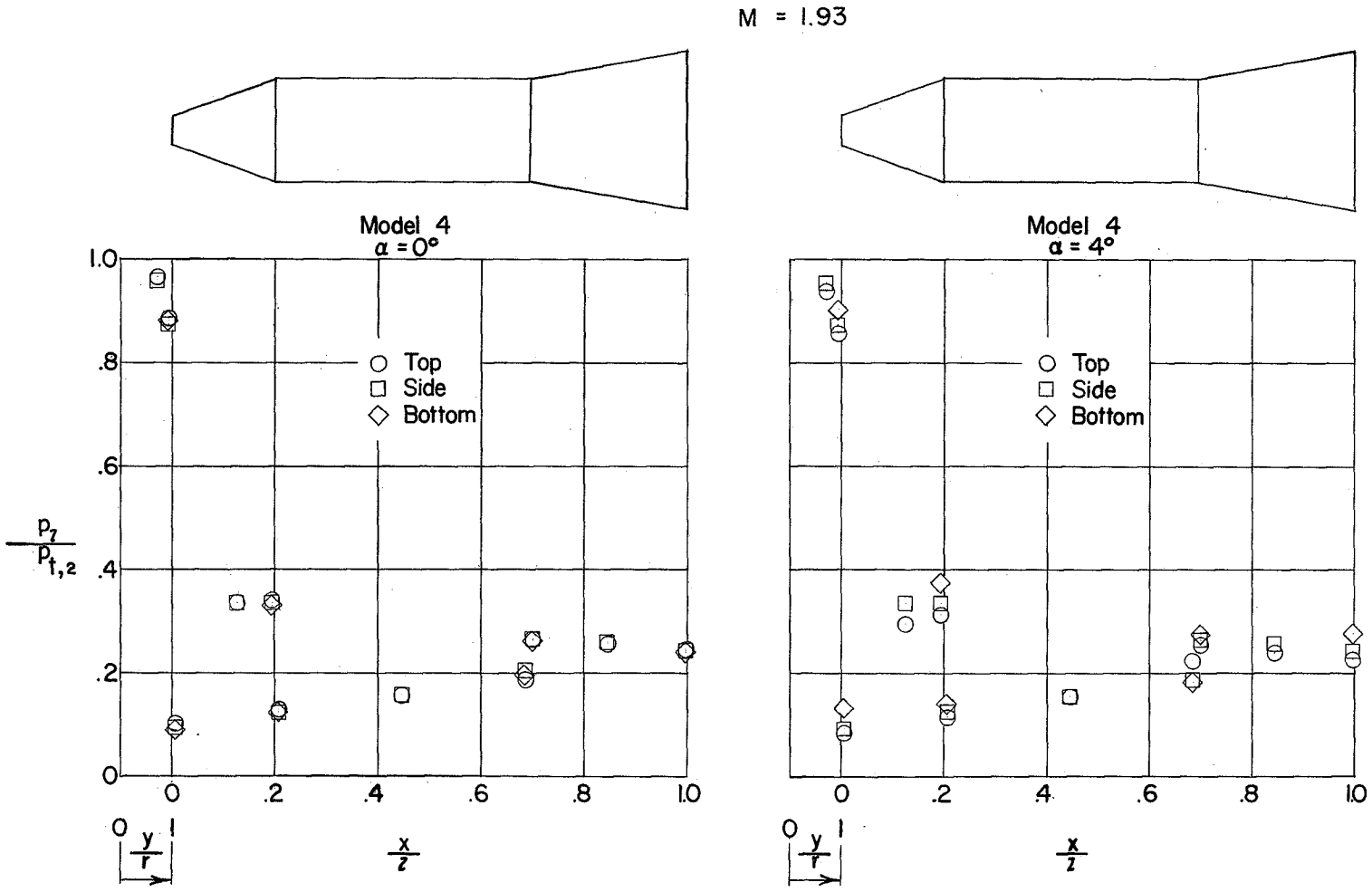

(a) $\alpha = 0^\circ$ and 4° at $M = 1.93$.

Figure 6.- Pressure measurements for model 4.

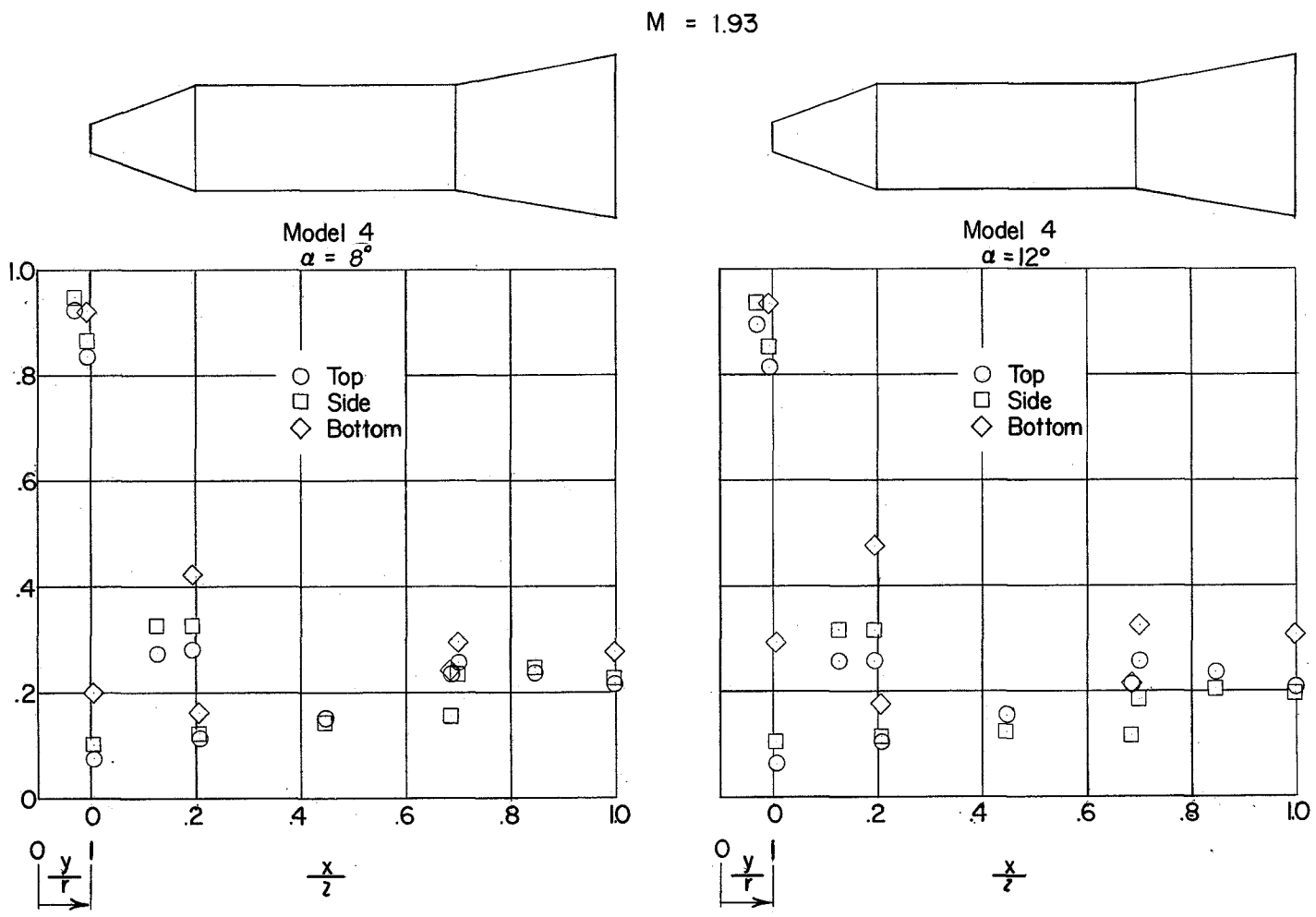

(b) $\alpha = 8^{\circ}$ and 12° at $M = 1.93$.

Figure 6.- Continued.

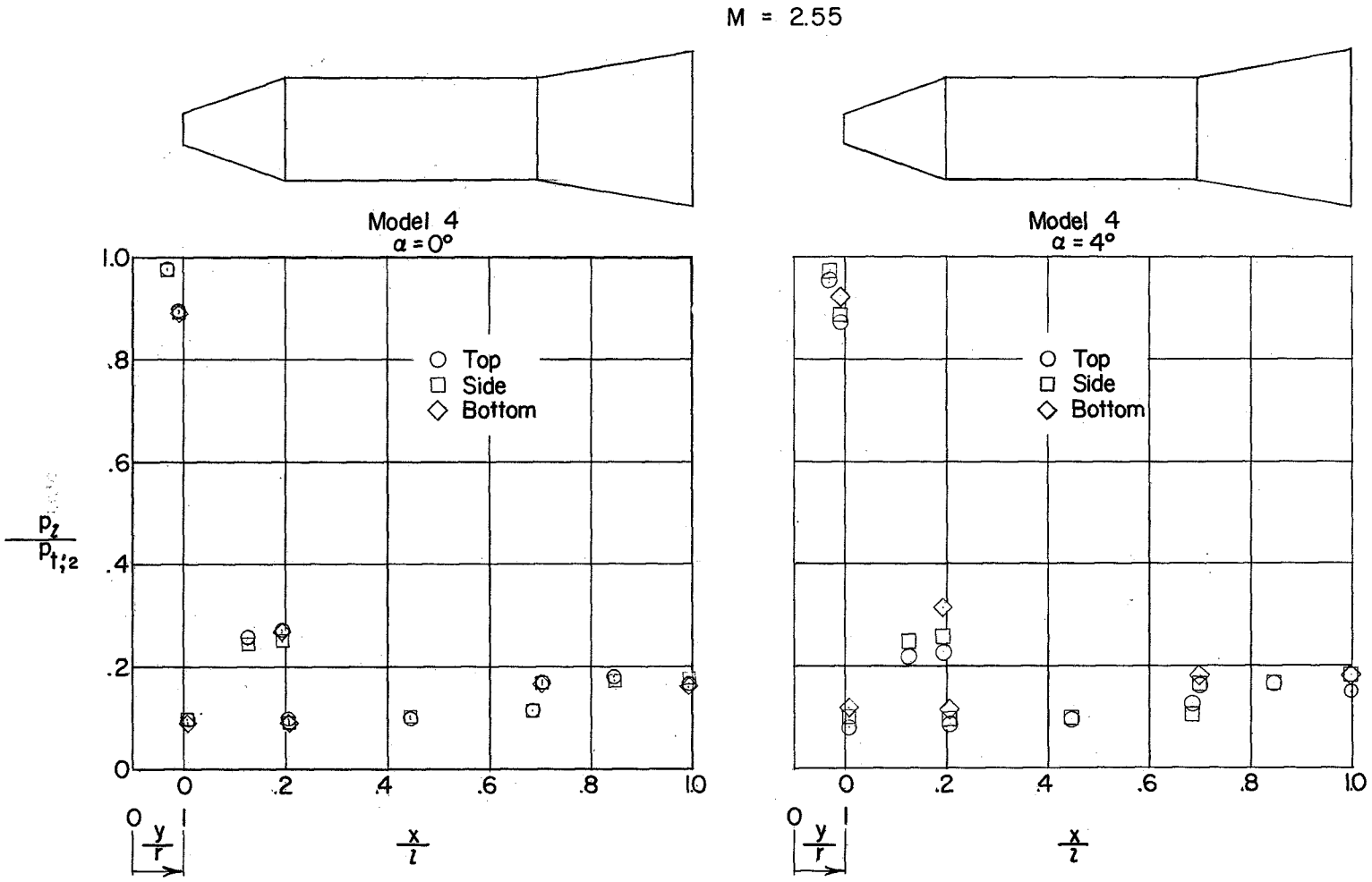

(c) $\alpha = 0^\circ$ and 4° at $M = 2.55$.

Figure 6.- Continued.

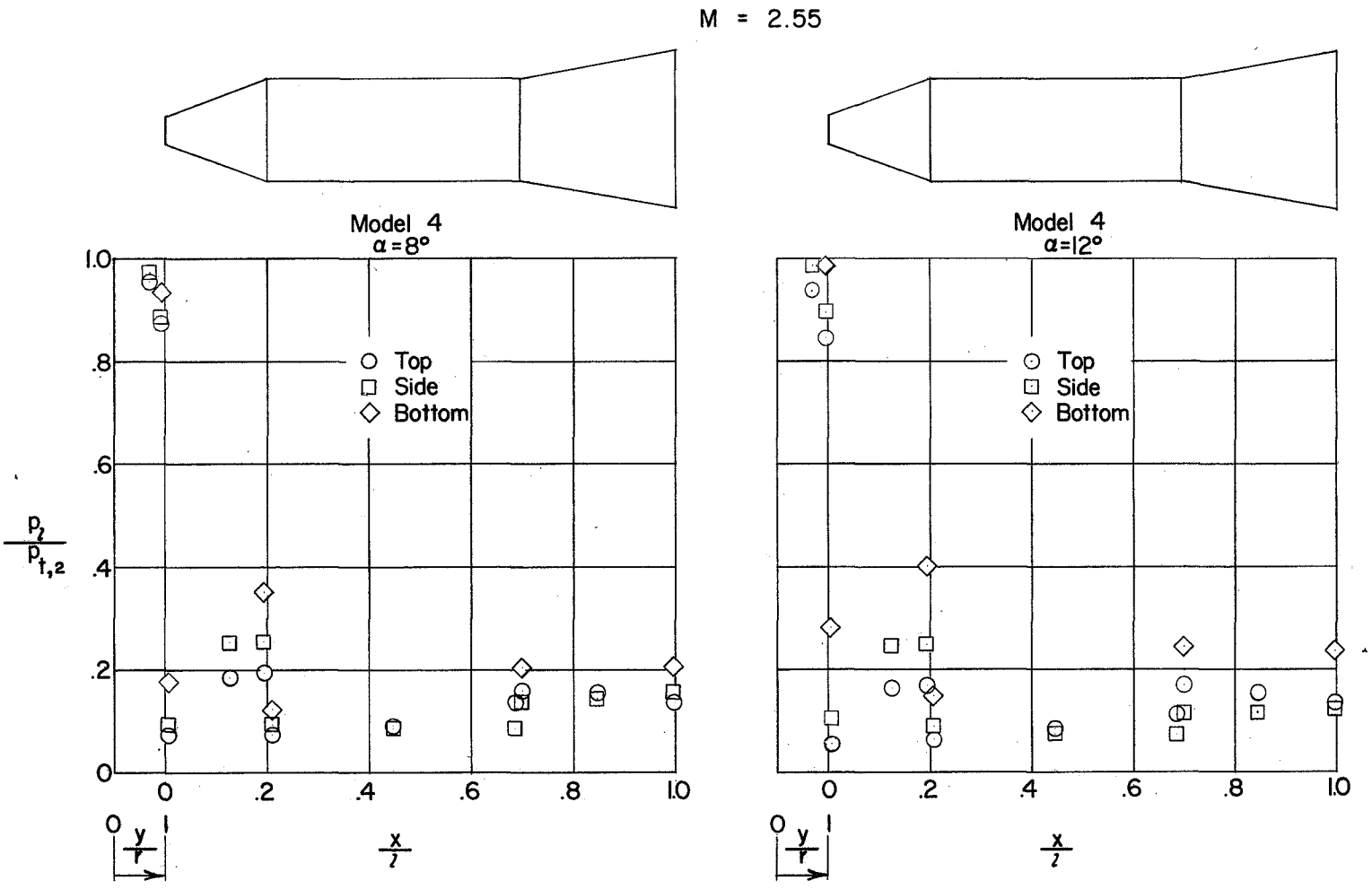

(d) $\alpha = 8^{\circ}$ and 12° at $M = 2.55$.

Figure 6.- Continued.

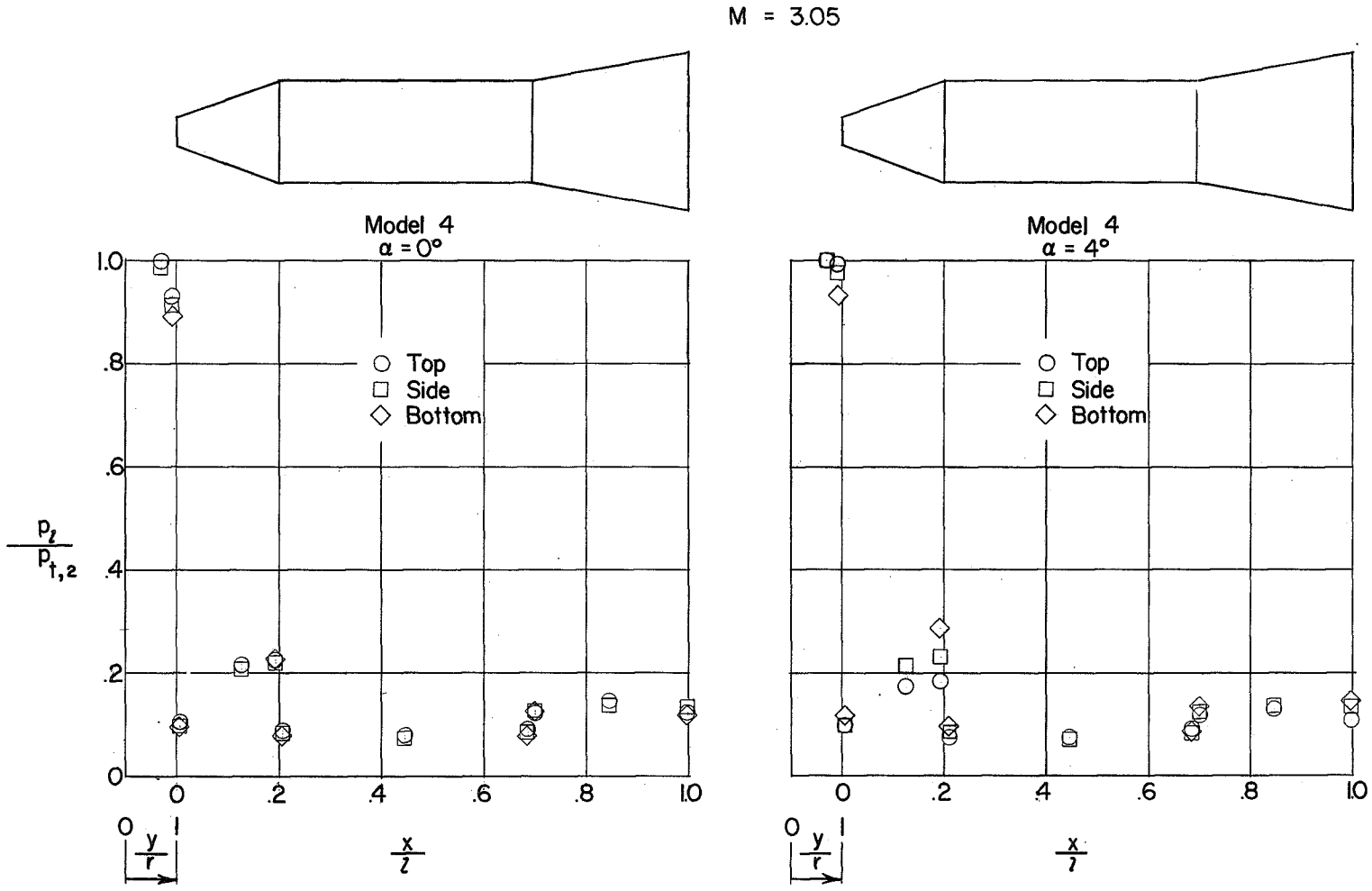

(e) $\alpha = 0^\circ$ and 4° at $M = 3.05$.

Figure 6.- Continued.

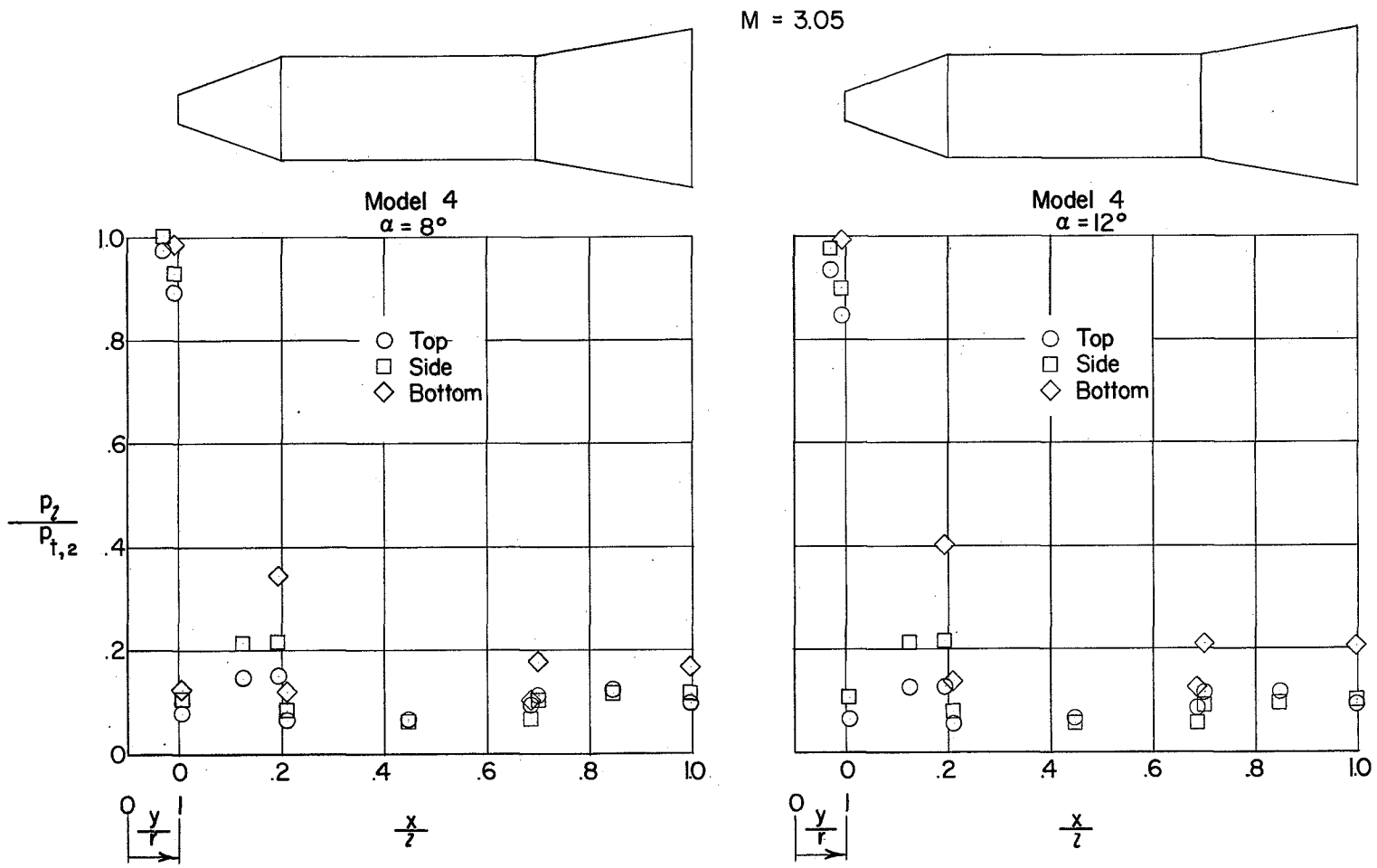

(f) $\alpha = 8^\circ$ and 12° at $M = 3.05$.

Figure 6.- Concluded.

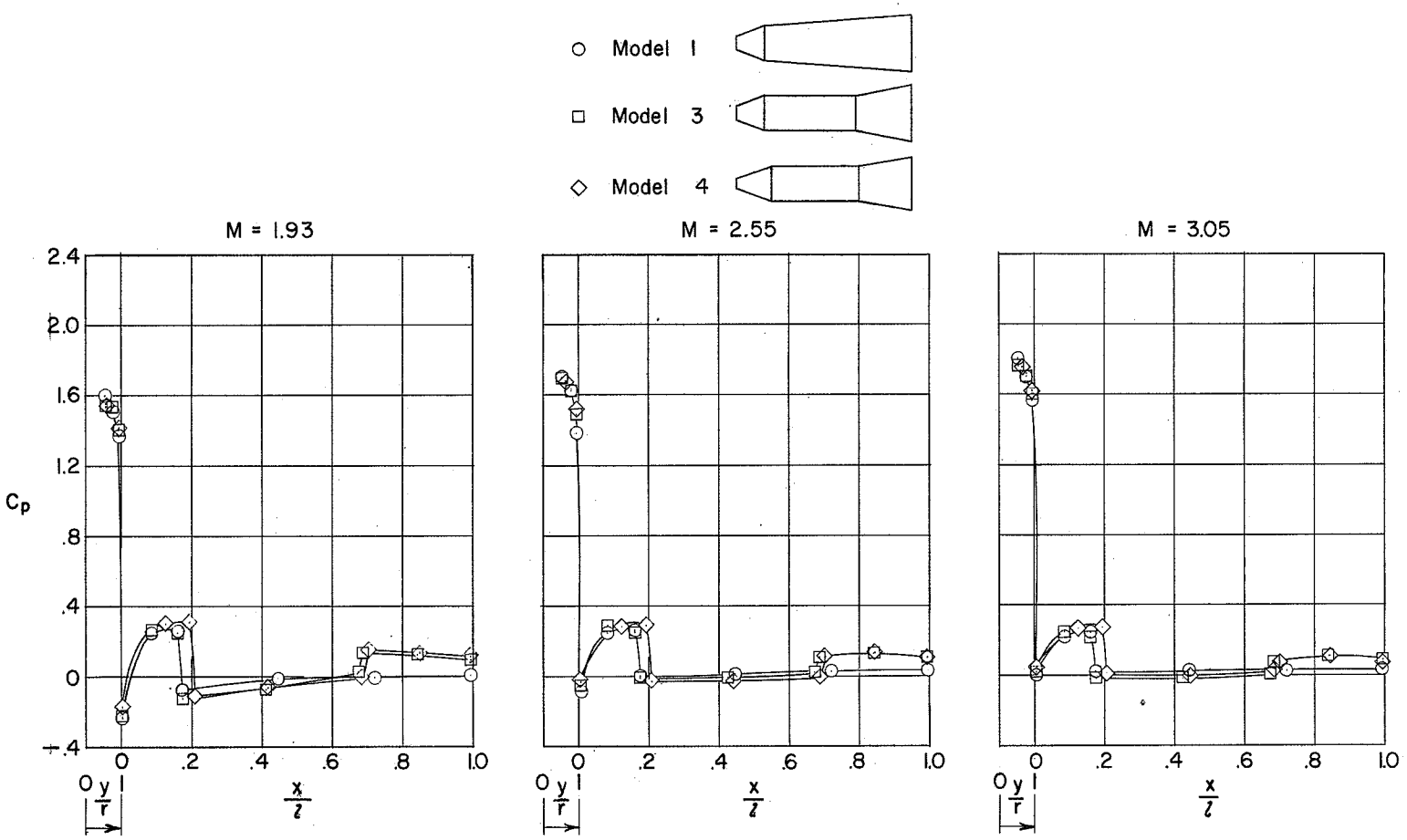

Figure 7.- Comparison of the pressure coefficients for the three models at $\alpha = 0^{\circ}$.

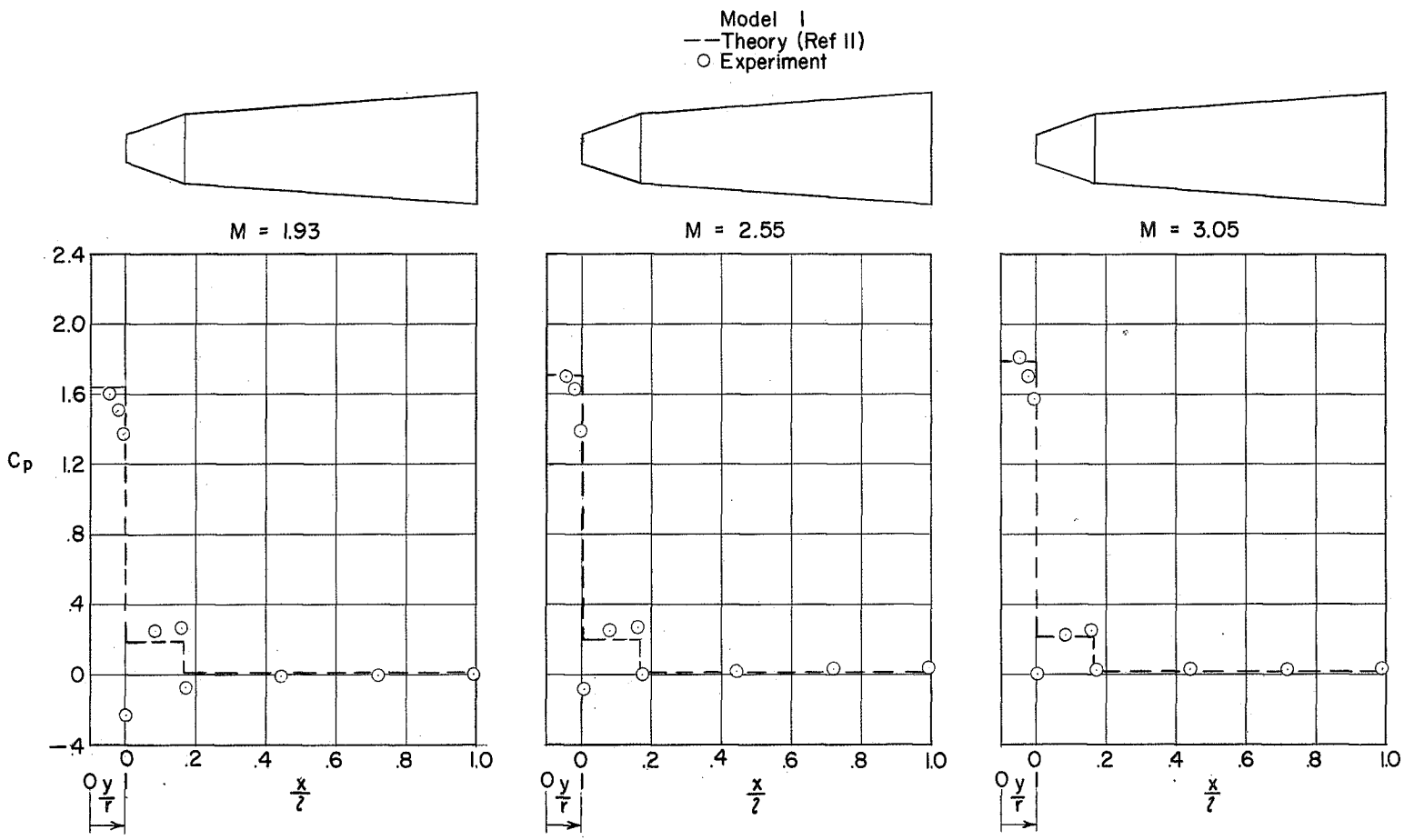

(a) Model 1.

Figure 8.- Comparison of the measured pressure coefficients with modified Newtonian theory at $\alpha = 0^{o}$.

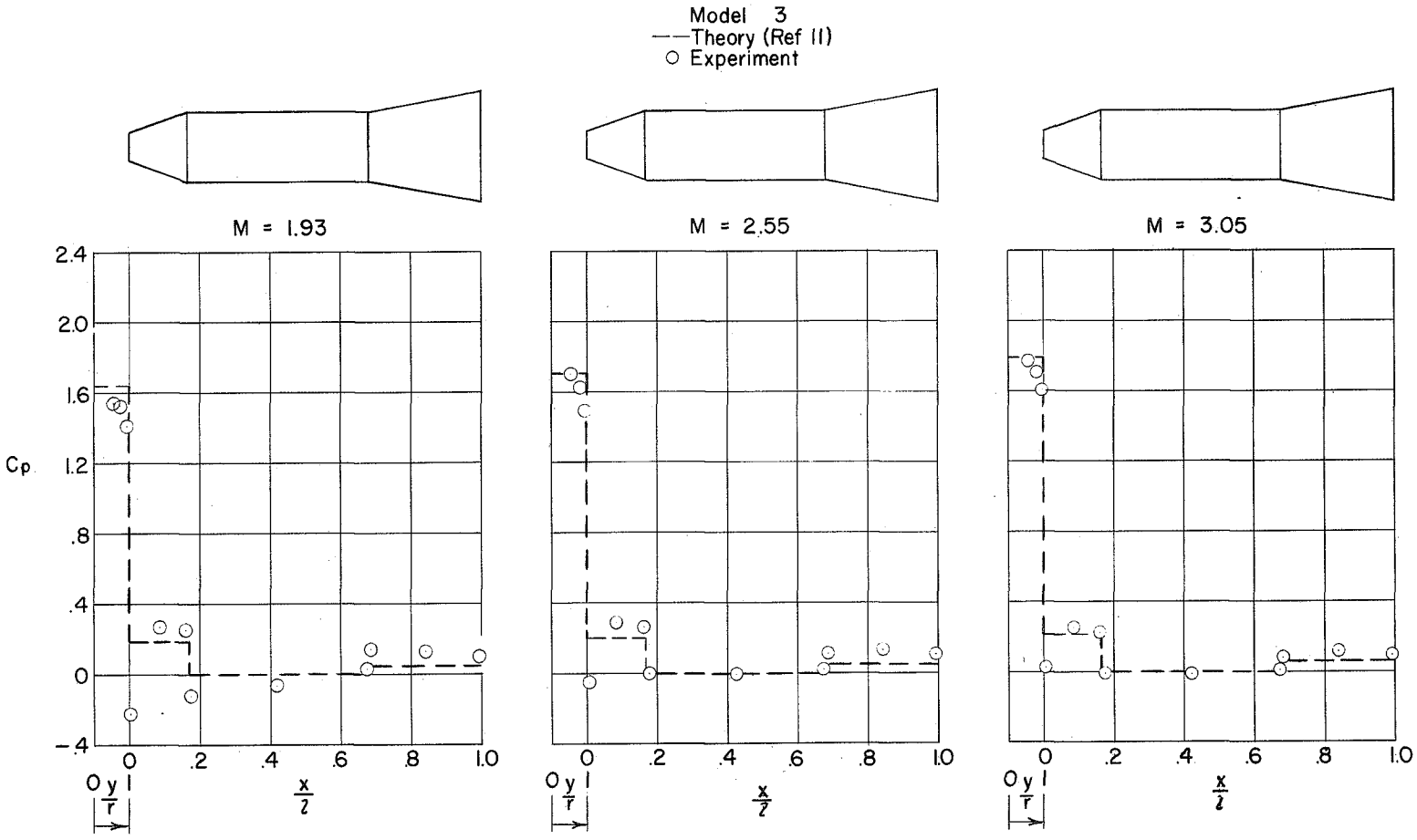

(b) Model 3.

Figure 8.- Continued.

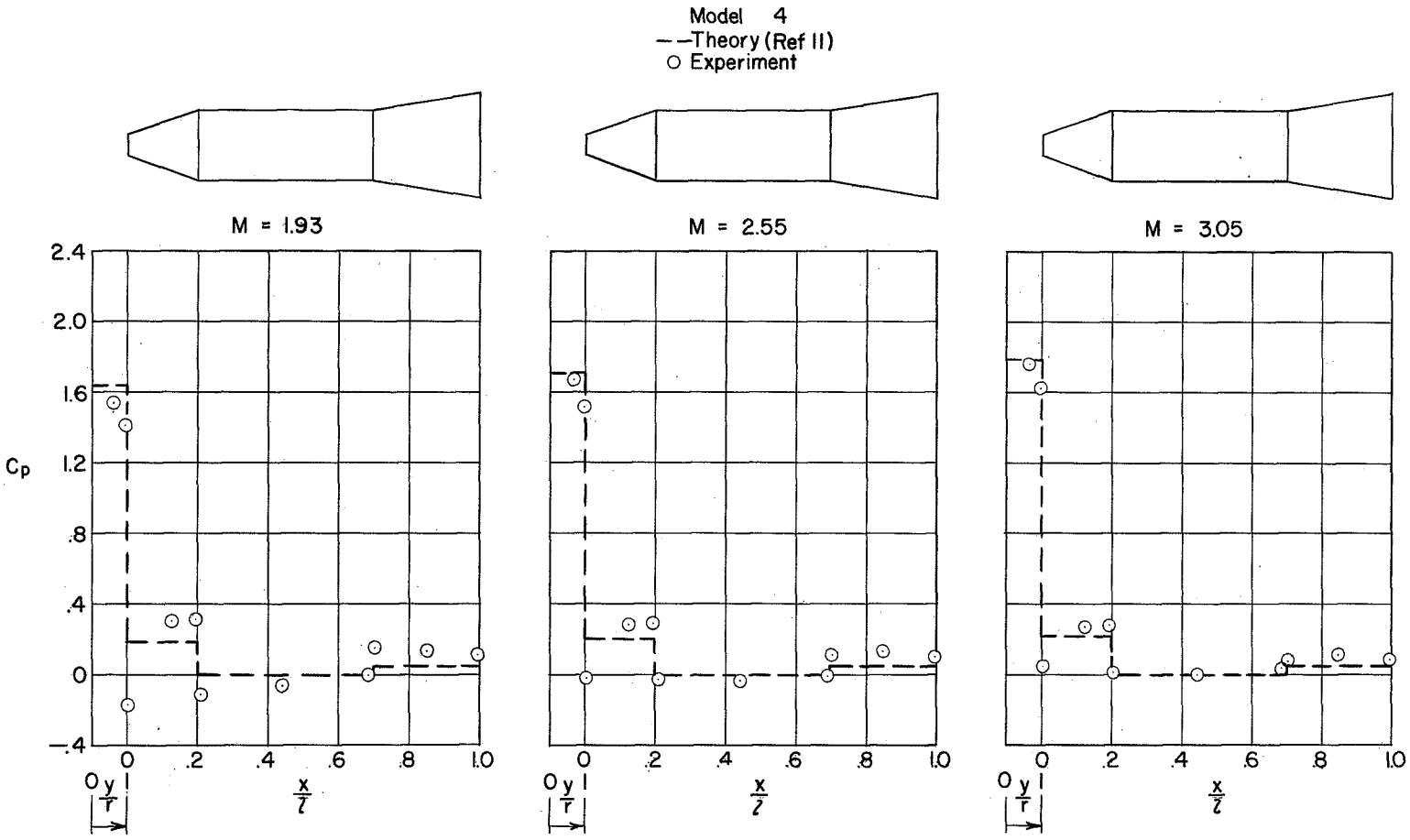

(c) Model 4.

Figure 8.- Concluded.

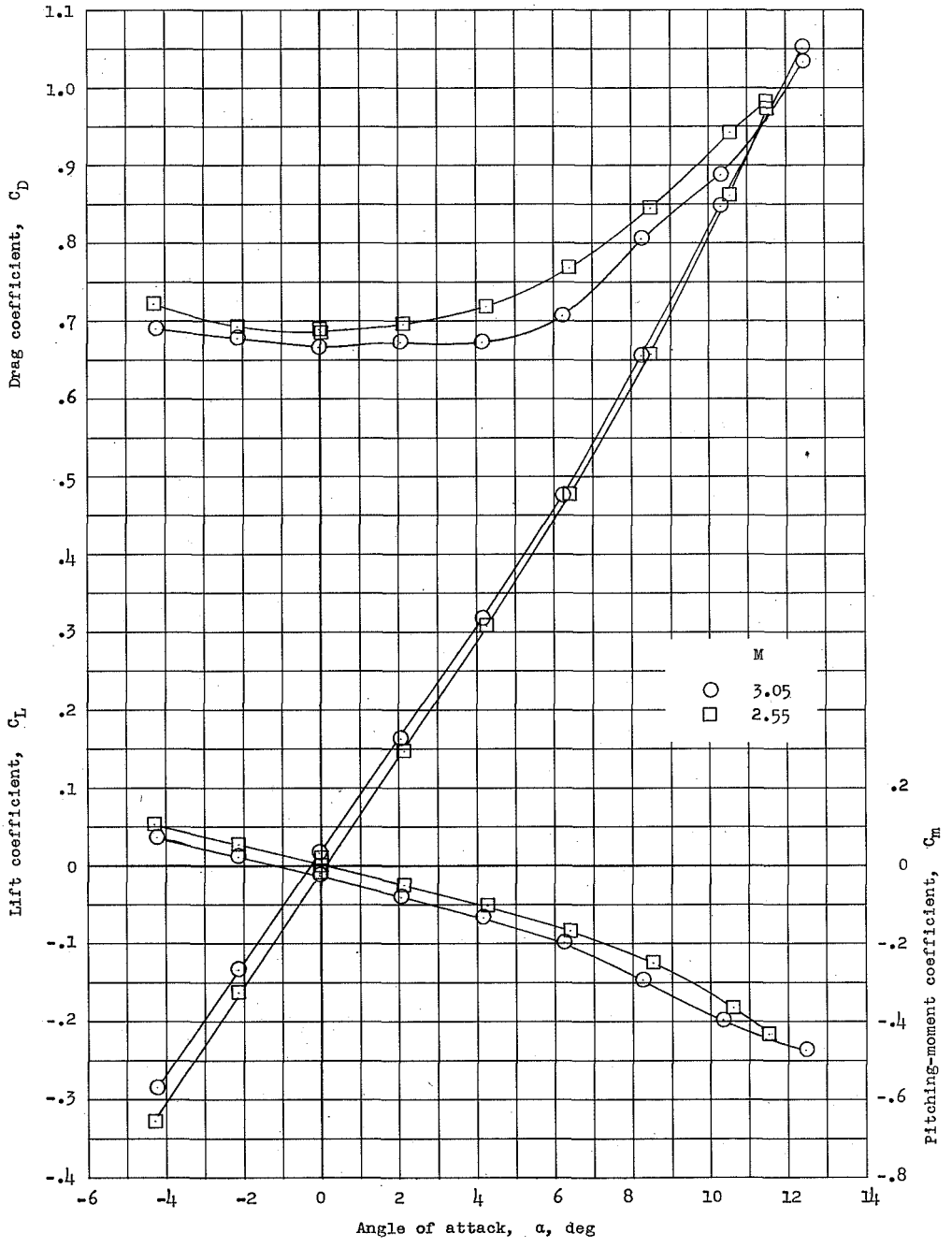

(a) Model 1.

Figure 9.- Force measurements for the three models at Mach numbers 2.55 and 3.05.

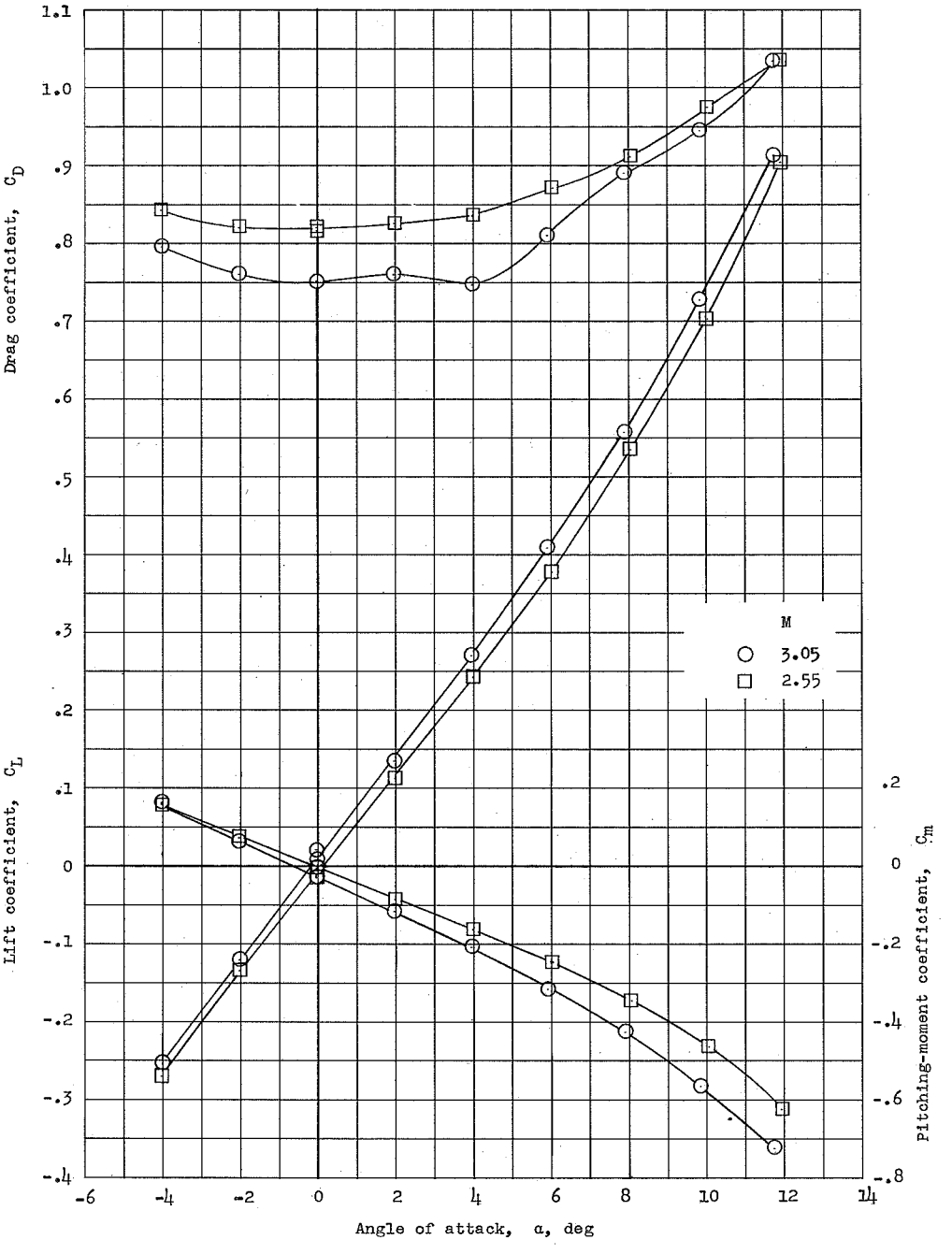

(b) Model 3.

Figure 9.- Continued.

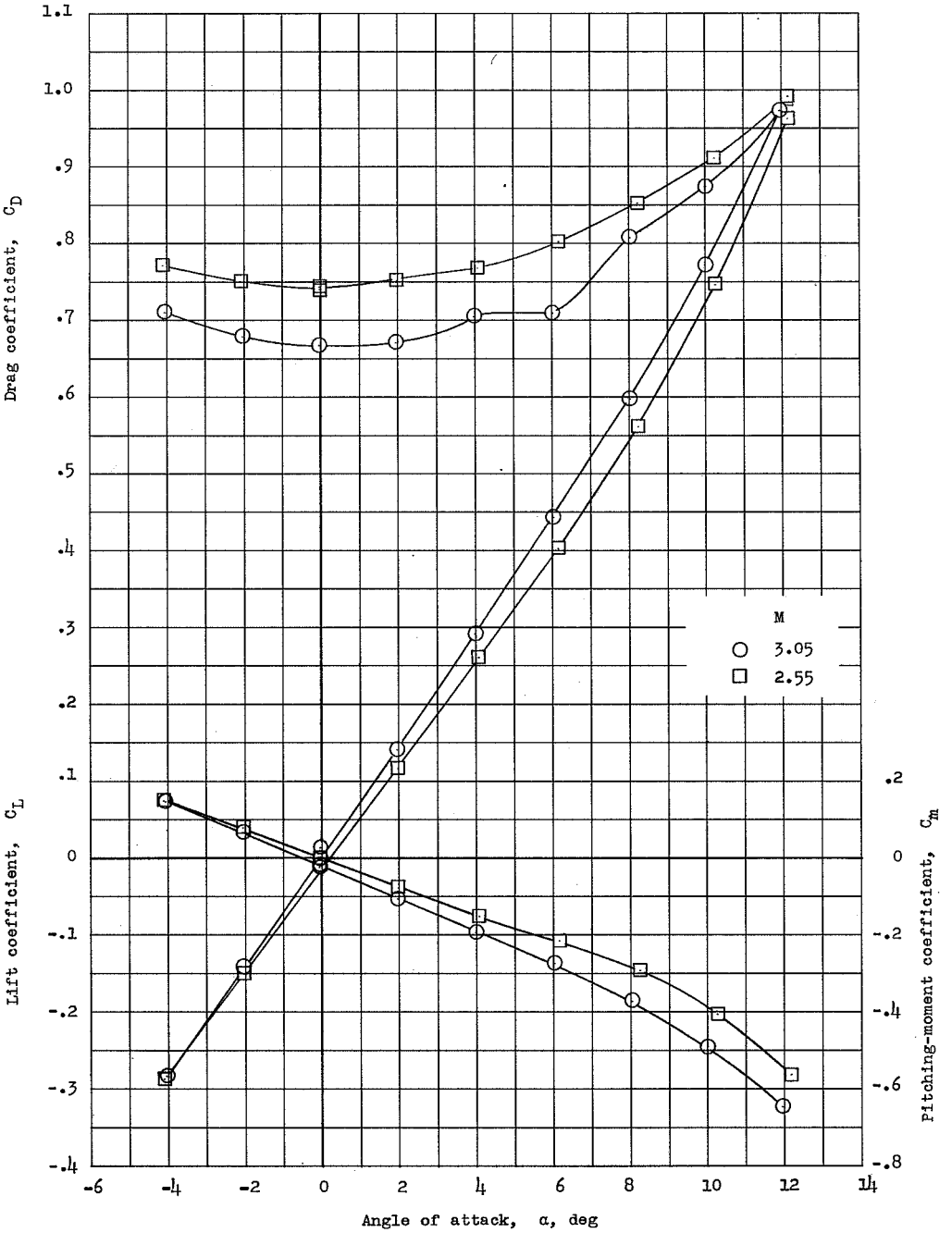

(c) Model 4.

Figure 9.- Concluded.

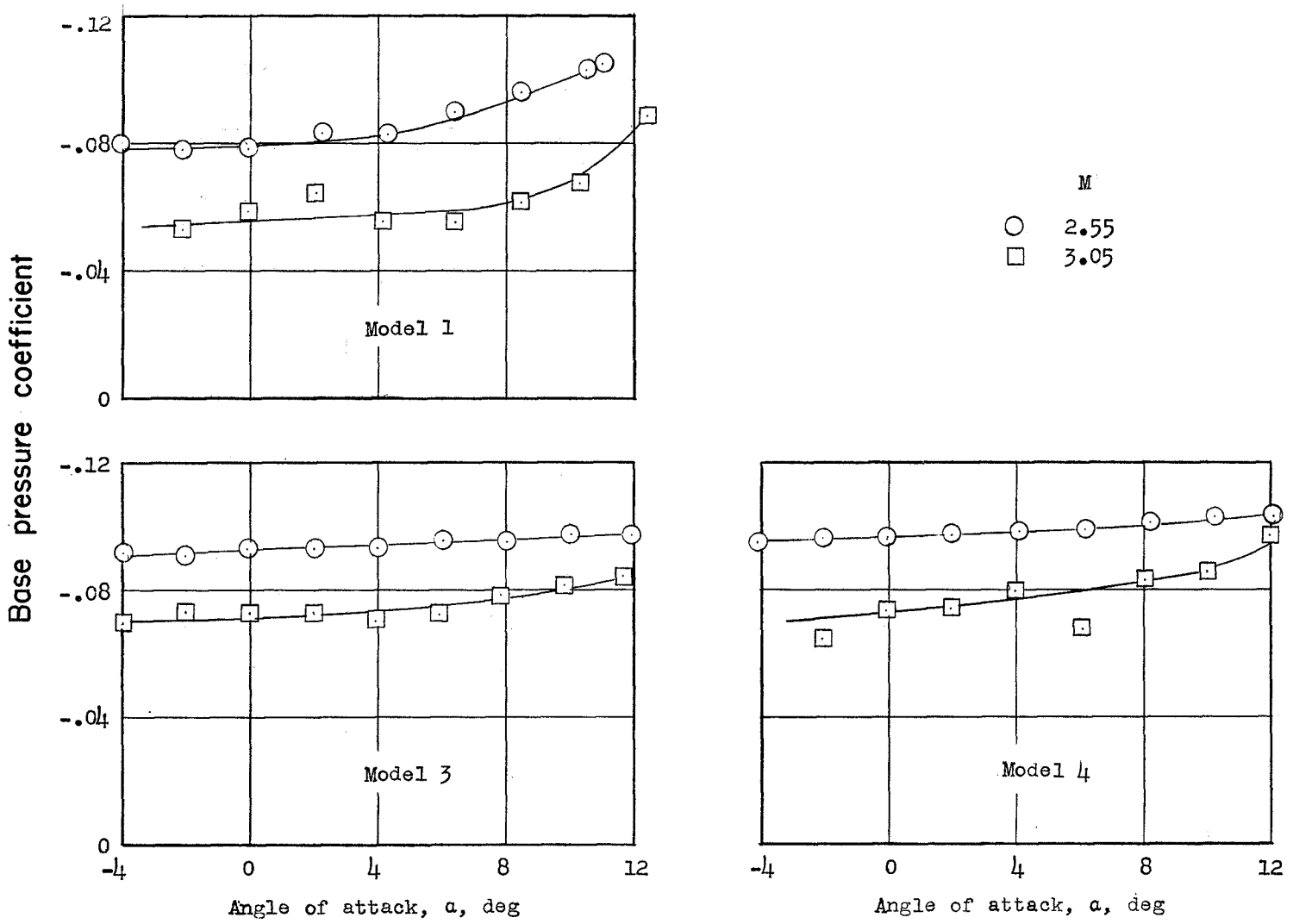

Figure 10.- The base pressure coefficients for the three models at M = 2.55 and 3.05.